Atmospheric
Chemistry
and Physics
Discussions

1 # Quantification of solid fuel combustion and aqueous chemistry
2 # contributions to secondary organic aerosol during wintertime
3 # haze events in Beijing

4 **Yandong Tong[1], Veronika Pospisilova[1,a], Lu Qi[1], Jing Duan[2], Yifang Gu[2], Varun Kumar[1],**
5 **Pragati Rai[1], Giulia Stefenelli[1], Liwei Wang[1], Ying Wang[2], Haobin Zhong[2], Urs Baltensperger[1],**
6 **Junji Cao[2], Ru-Jin. Huang[2], Andre Stephan Henry Prevot[1], and Jay Gates Slowik[1]**

7 [1]Laboratory of Atmospheric Chemistry, Paul Scherrer Institute (PSI), 5232 Villigen, Switzerland

8 [2]Key Lab of Aerosol Chemistry & Physics, Institute of Earth Environment, Chinese Academy of
9 Sciences, Xi'an, China

10 [a]now at: Tofwerk AG, Uttigenstrasse 22, 3600 Thun, Switzerland

11 **Correspondence: J. G. Slowik (jay.slowik@psi.ch)**

12 **Abstract:** In recent years, intense haze events in megacities such as Beijing have received significant
13 study. Although secondary organic aerosol (SOA) has been identified as a major contributor to such
14 events, knowledge of its sources and formation mechanisms remains uncertain. We investigate this
15 question through the first field deployment of the extractive electrospray ionisation time-of-flight
16 mass spectrometer (EESI-TOF-MS) in Beijing, together with an Aerodyne long time-of-flight aerosol
17 mass spectrometer (L-TOF AMS). Measurements were performed during autumn and winter 2017,
18 capturing the transition from non-heating to heating seasons. Source apportionment resolved four
19 factors related to primary organic aerosols (traffic, cooking, biomass burning, and coal combustion),
20 as well as four related to secondary organic aerosol (SOA). Of the SOA factors, two were related to
21 solid fuel combustion (SFC), one to SOA generated from aqueous chemistry, and one to
22 mixed/indeterminate sources. The SFC factors were identified from spectral signatures corresponding
23 to aromatic oxidation products, while the aqueous SOA factor was characterised by signatures of
24 small organic acids and diacids, and unusually low CO^+/CO_2^+ fragment ratios measured by the AMS.
25 Solid fuel combustion was the dominant source of SOA during the heating season. However, a
26 comparably intense haze event was also observed in the non-heating season, and was dominated by
27 the aqueous SOA factor. Aqueous chemistry was promoted by the combination of high relative
28 humidity and air masses passing over high NO_x regions to the south and east of Beijing, leading to
29 high particulate nitrate. The resulting high liquid water content was highly correlated with the
30 concentration of the aqueous SOA factor. These results highlight the strong compositional variability
31 between different haze events, indicating the need to consider multiple formation pathways and
32 precursor sources to describe SOA during intense haze events in Beijing.

33

34 ## 1. Introduction

35 Atmospheric aerosols negatively affect human health (Beelen et al., 2014; Laden et al., 2006; Pope et
36 al., 2002), visibility (Chow et al., 2002), and urban air quality (Fenger, 1999; Mayer, 1999) on local
37 and regional scales. Aerosols are also linked to the most important uncertainties with regards to global
38 radiation balance and climate change (Myhre et al., 2014; Penner et al., 2011; Forster et al., 2007;
39 Lohmann and Feichter, 2005). Organic aerosol (OA) is a major component of atmospheric aerosol
40 and contributes significantly to the total aerosol mass (Jimenez et al., 2009). OA sources are typically
41 classified as either primary organic aerosol (POA), which is directly emitted from sources such as
42 fossil fuel combustion, industrial emissions, biomass burning and cooking emissions, or secondary
43 organic aerosol (SOA), which is produced by atmospheric oxidation of volatile organic compounds
44 (VOCs), yielding lower-volatility products that can subsequently partition to the particle phase.

1   Overall, SOA accounts for approximately from 20 % to 90 % of total OA (Jimenez et al., 2009). The
2   health effects resulting from primary and secondary aerosols have drawn public attention in recent
3   years. For example, exposure to primary wood burning aerosol is associated with increased risk of
4   respiratory disease and may cause adverse effects to airway epithelia (Liu et al., 2017a; Krapf et al.,
5   2017). SOA has the potential for inducing reactive oxygen species (ROS); these can be linked to
6   inflammation and oxidative stress at high concentration (Reuter et al., 2010; Li et al., 2003), which in
7   turn can cause oxidative damage to proteins and DNA within cells (Halliwell and Cross, 1994).
8   Therefore, understanding the aerosol sources becomes essential. Previous studies have been relatively
9   successful in quantitatively linking POA to its sources, However, quantification of SOA sources
10 and/or formation pathways is much more challenging, because SOA consists of thousands of
11 multifunctional, highly oxygenated compounds, including high molecular weight species and
12 oligomers, which are difficult to measure using traditional instrumentation. Therefore, the effects of
13 individual SOA sources on health and climate remain poorly constrained.

14 Air pollution problems caused by high concentration of fine particles are of great concern in many
15 Chinese cities, including Beijing. In 2013, the Chinese government introduced the "Atmospheric
16 Pollution Prevention and Control Action Plan", a five-year plan to aggressively control anthropogenic
17 emissions and $PM_{2.5}$ concentration. Although the annual mean concentration of $PM_{2.5}$ in Beijing
18 decreased from 90 µg m^{-3} in 2013 to 58 µg m^{-3} in 2017, it remains much higher than the Chinese
19 National Ambient Air Quality Standard (CNAAQS, 35 µg m^{-3} as an annual mean $PM_{2.5}$ concentration)
20 and the World Health Organisation (WHO) guidelines (10 µg m^{-3} as an annual mean $PM_{2.5}$
21 concentration). Also, extreme haze events are still very frequent in northern China (An et al., 2019).
22 Extensive studies conducted in Beijing in recent years investigated the chemical composition and
23 sources of fine particles by different online and offline analytical methods (Duan et al., 2020; Duan et
24 al., 2019; Xu et al., 2019; Zhao et al., 2019; Äijälä et al., 2017; Elser et al., 2016; Hu et al., 2016; Sun
25 et al., 2016a; Huang et al., 2014; Zhang et al., 2014; Sun et al., 2013). Among these studies, aerosol
26 mass spectrometers (AMS) equipped with a PM_1 aerodynamic lens are widely used due to their robust
27 quantification ability. In these studies, POA factors are separated and well-understood. Coal
28 combustion aerosol was found to be one of the most important POA sources in winter, with mean
29 contributions ranging from 10 % to 30 %. Primary biomass burning emissions contributed
30 approximately 9 % to 18 % of OA. Traffic and cooking were also consistently identified as significant
31 POA sources, comprising 9 % to 18 % and 12 % to 20 %, respectively, of OA. SOA comprises about
32 35 % to 70 % of total OA in Beijing, but apportionment to specific sources and/or formation
33 processes has not been achieved yet in Beijing. This is typical of AMS measurements, which in most
34 studies report either a single SOA factor (denoted oxygenated organic aerosol, OOA), or two factors
35 distinguished by the extent of oxygenation (less oxygenated OOA, LO-OOA, and more oxygenated
36 OOA, MO-OOA) (Xu et al., 2019; Elser et al., 2016; Sun et al., 2016a; Sun et al., 2013). These
37 factors have alternatively been described in terms of volatility as semi-volatile OOA (SV-OOA) and
38 low-volatility OOA (LV-OOA), respectively (Zhao et al., 2019; Zhang et al., 2014; Hu et al., 2013).
39 The main exceptions to this descriptive framework for SOA include SOA from oxidation of isoprene
40 epoxydiols (Budisulistiorini et al., 2013) and long-term measurements in Europe by online ACSM
41 and/or offline AMS that show systematic differences in SOA factors retrieved during different
42 seasons. These differences have been attributed to the relative importance of biogenic SOA in summer
43 vs. SOA from domestic wood combustion in winter, although this attribution rests on temporal
44 correlations with external tracer measurements and knowledge of source seasonality rather than
45 specific AMS spectral markers (Bozzetti et al., 2017; Daellenbach et al., 2017). As a result, the main
46 contributors to SOA in Beijing (and other megacities) remain a source of significant uncertainty,
47 which continues to hinder the development of effective mitigation strategies.

48 OA composition is measured either by filter sampling followed by offline laboratory analyses or by
49 online, real-time instrumentation. Offline filter analysis has some advantages, including 1) possibility
50 to apply a wide variety of analytical techniques, which can maximise the chemical information

1   retrieved for the analysed fraction; and 2) low cost and maintenance requirements for filter sampling,
2   which in turn facilitates 3) practicality of wide spatial and temporal coverage. However, it also has
3   some drawbacks, including 1) low time resolution incapable of capturing characteristic timescales of
4   certain OA sources and/or ageing and formation processes; 2) artefacts due to adsorption, evaporation,
5   and chemical reactions during sample collection, storage, and/or transfer, (Ge et al., 2012; Huang et
6   al., 2010; Hildebrandt et al., 2010; Hallquist et al., 2009); 3) the analysable OA faction may vary
7   significantly between different techniques. Current online real-time aerosol speciation techniques
8   provide higher time resolution, but have typically required trade-offs between chemical resolution,
9   time resolution, and/or detectable mass fraction. For example, the Aerodyne aerosol mass
10   spectrometer (AMS) provides quantitative NR-PM$_{2.5}$ chemical composition (including sulphate,
11   nitrate, ammonium, chloride and organic) with time resolution on the order of 1 min. These
12   quantitative and highly time-resolved measurements are facilitated by high temperature vaporisation
13   (600 $^\circ$C) and high energy ionisation (electron ionisation at 70 eV) (DeCarlo et al., 2006), which induce
14   significant thermal decomposition and ionisation-induced fragmentation. These processes destroy
15   chemical information of molecules beneficial for source apportionment, particularly for the
16   multifunctional and highly oxygenated molecules of which SOA is comprised. The CHARON PTR-
17   MS uses a lower temperature vaporisation scheme to avoid thermal decomposition, while maintaining
18   high time resolution, but the proton transfer reaction ionisation scheme is sufficiently energetic to
19   cause extensive fragmentation of typical SOA molecules (Muller et al., 2017; Eichler et al., 2015). To
20   reduce ionisation-induced fragmentation, several semi-continuous measurement techniques have also
21   been developed, e.g. Filter Inlet for Gases and AEROsols chemical ionisation time-of-flight mass
22   spectrometer (FIGAERO-CIMS) by Lopez-Hilfiker et al. (2014), and Thermal Desorption Aerosol
23   GC/MS-FID (TAG) by Williams et al. (2006). Although these instruments have lower thermal
24   decomposition and better chemical resolution, like offline filter sampling they are subject to
25   reaction/vaporisation processes on the collection substrate and decreased time resolution. Therefore,
26   to better quantify the SOA sources and/or formation processes, an instrument that can resolve aerosol
27   chemical composition at the molecular level with higher time resolution is required. The extractive
28   electrospray ionisation time-of-flight mass spectrometer (EESI-TOF-MS), developed at Paul Scherrer
29   Institut (PSI), provides online, near-molecular-level measurement (i.e., molecular formulae) of
30   organic aerosol composition with high time resolution of seconds without thermal decomposition or
31   ionisation-induced fragmentation (Lopez-Hilfiker et al., 2019). Two recent source apportionment
32   studies in Zurich using an EESI-TOF, together with an AMS, successfully resolved several SOA
33   factors and quantified the processes governing SOA concentrations (Qi et al., 2019; Stefenelli et al.,
34   2019). These studies confirm that the combination of EESI-TOF and AMS is highly complementary,
35   with the AMS providing robust quantification but limited chemical resolution, and the EESI-TOF
36   providing a linear but hard-to-quantify response with high chemical resolution. The combined
37   measurements, therefore, has the potential to provide quantitative, real-time measurement of organic
38   aerosol composition with high chemical resolution.

39   Here we present AMS and EESI-TOF measurements in Beijing from late September to mid-
40   December 2017. This campaign captures distinct characteristics of the non-heating season and heating
41   season, which begins on 15 November. An integrated source apportionment analysis of AMS and
42   EESI-TOF data is performed to characterise the sources and physicochemical processes governing
43   SOA composition.

44

45   **2. Methodologies**
46   **2.1 Measurement campaign**

47   Measurements were conducted at the National Centre for Nanoscience and Technology in Beijing
48   (40.00º N, 116.38º E). Beijing is the capital city of China PR and one of the most populated cities in

1   the world, with more than 20 million inhabitants. It is located at the northwestern end of the North
2   China Plain and surrounded by the Yan Mountains from the southwest to the northeast. The
3   measurement site is located on the roof of the South Building of the National Centre for Nanoscience
4   and Technology (~20 m above ground level) surrounded by smaller buildings, with the exception of
5   an 18-floor building approximately 30 m to the north, which may interfere and even block the wind
6   from this direction. The northern part of the fourth ring highway is situated about 200 m way to the
7   south of the site, however, between the highway and the site, there are several buildings, which reduce
8   the influence from highway traffic. This location is not affected by major emissions from industries.

9   The measurements took place from late September to mid-December, 2017. Here we focus on OA
10   measurements from late October to mid-December, 2017, conducted by an extractive electrospray
11   ionisation long time-of-flight mass spectrometer (EESI L-TOF MS) and a long time-of-flight aerosol
12   mass spectrometer (L-TOF AMS). A scanning mobility particle sizer (SMPS) was additionally
13   deployed at the site to measure particle size distribution. Ambient air was sampled through a $PM_{2.5}$
14   cyclone to remove coarse particles ($\sim$ 50 cm above the roof of the measurement site building). The air
15   passed through a stainless steel ($\sim$ 6 mm outer diameter and $\sim$ 4 mm inner diameter) tube into the
16   EESI L-TOF MS, L-TOF AMS, and SMPS, installed on the same line and in close proximity.

17   **2.2 Instrumentation**
18   2.2.1   Extractive electrospray ionisation long time-of-flight mass spectrometer (EESI-
19   TOF)

20   The EESI-TOF provides online, highly time-resolved measurements of the organic aerosol molecular
21   ions without thermal decomposition or ionisation-induced fragmentation. A detailed description can
22   be found elsewhere (Lopez-Hilfiker et al., 2019). The system used in this campaign consists of a
23   recently developed EESI source integrated with a commercial long-time-of-flight (LTOF) mass
24   spectrometer (Tofwerk AG, Thun, Switzerland), which in this campaign achieved mass resolution of
25   ~8000 Th Th^{-1} at mass to charge ratios m/z higher than 170. The EESI-TOF continuously sampled at
26   ~0.8 L min^{-1}, alternating between direct ambient sampling (15 min) and sampling through a particle
27   filter (5 min) to obtain a measurement of the instrument background. The ambient spectrum (M_{total})
28   minus the average of the immediately adjacent background spectra (before and after) (M_{filter}) yields a
29   difference spectrum taken as the ambient aerosol composition (M_{diff}). In both modes, the sampled air
30   passes through a multi-channel extruded carbon denuder (with diameter of 4 mm and length of 3 to 4
31   cm) which eliminates negative artefacts from semi-volatile species desorbing from the particle filter
32   and positive artefacts when the particle filter acts as a sink of semi-volatile species, and also improves
33   detection limits by reducing the gas-phase background. Particles then intersect a spray of charged
34   droplets generated by a conventional electrospray probe and the soluble fraction is extracted into the
35   solvent. Then the droplets pass through a heated stainless-steel capillary (~250 ◦C), wherein the
36   electrospray solvent evaporates and ions are ejected into the mass spectrometer. Due to short
37   residence time (~1 ms) in the capillary, no thermal decomposition is observed. Finally, the ions are
38   analysed by a portable high resolution time-of-flight mass spectrometer with an atmospheric pressure
39   interface (API-TOF) (Junninen et al., 2010). In this campaign, the electrospray consisted of a 1:1
40   water/acetonitrile mixture doped with 100 ppm NaI, and the mass spectrometer was configured to
41   detect positive ions. Ions are detected in the form of $[M]Na^+$ (where M is the analyte) and other
42   ionisation pathways are mostly suppressed, yielding a linear response to mass (without significant
43   matrix effects) and simplifying spectral interpretation (Lopez-Hilfiker et al., 2019).

44   The high pollution levels experienced during this campaign presented several operational and
45   analytical challenges for the EESI-TOF, specifically: (1) denuder break-through, which increased
46   background signal, led to the detection of spurious signals in the particle phase, and increased the time
47   required to achieve a stable signal following a filter switch between M_{total} and M_{filter}; (2) prevalence of
48   large particles during haze events; and (3) increase in the required frequency of cleaning (unclogging)

1 and realigning the electrospray capillary. These issues are discussed below in conjunction with the
2 operational and data analysis protocols.

3 The EESI-TOF achieved ~ 90 % data coverage during the sampling period, with the 10 % missing
4 data including solution changes, signal loss due to electrospray capillary clogging, interruption by
5 periodic maintenance (e.g. to clean the ESI and capillary into the TOF and to regenerate the denuder)
6 and calibration by nebulising levoglucosan aerosol to quantify the mass concentration with an SMPS
7 after each haze event (typically three to four days). Although the calibration by levoglucosan could
8 indicate the instrument's linear response to mass concentration, the sensitivity to levoglucosan was
9 found to be different in between different haze events because of the interruption. Therefore, a
10 diagnostic species that can be measured with higher time resolution is utilised to monitor the
11 sensitivity throughout the campaign. Intercomparison of inorganic nitrate species between AMS and
12 EESI-TOF yieded strong correlations during periods in which the instrument operation was stable
13 (i.e., not affected by major clogging or cleaning/realignment of the electrospray capillary). Note that
14 these issues are expected to result in changes in EESI-TOF sensitivity that uniformly affect all
15 measured ions (i.e., without compound-dependent effects). Therefore, we correct for these effects by
16 normalizing the EESI-TOF signal using a comparison of the nitrate signal ([NaNO$_3$]Na$^+$) from the
17 EESI-TOF and the nitrate concentration (NO$_3^-$) from the AMS (Fig. S1). The whole campaign was
18 divided into different periods, and the slope of linear fit between EESI-TOF nitrate signal and AMS
19 nitrate concentration in each period was taken as the sensitivity of EESI-TOF to nitrate in this period
20 as shown in Eq. (1a). The time period from 3 to 7 November was selected as a reference period and
21 the sensitivity determined in other periods (k_q, with q denoting the individual periods) was normalised
22 to the sensitivity of reference period (k_{ref}). Finally, the data collected from EESI-TOF was normalised
23 according to Eq. (1b)

24
$$k_q = \left(\frac{I_{[NaNO_3]Na^+,EESI-TOF}}{I_{NO_3^-,AMS}} \right)_q \quad (1a)$$

25
$$I'_{i,j,q} = I_{i,j,q} \times \frac{k_{ref}}{k_q} \quad (1b)$$

26 Here $I_{[NaNO_3]Na^+,EESI-TOF}$ and $I_{NO_3^-,AMS}$ are the signal of [NaNO$_3$]Na$^+$ and NO$_3^-$ collected by EESI-
27 TOF and AMS, respectively in Eq. (1a). In Eq. (1b), $I'_{i,j,q}$ and $I_{i,j,q}$ indicate the signal of the ith ion at
28 time point j in pth period after and before normalisation, respectively, and k_{ref} is the reference
29 sensitivity. After normalisation, time-dependent changes in sensitivity are eliminated for nitrate and,
30 we assume, for organics.

31 In the conventional EESI-TOF setup, the denuder is positioned less than 1 cm away from the
32 electrospray probe (Lopez-Hilfiker et al., 2019). In this campaign, we found that this configuration led
33 to significant losses of large particles. This was inferred from investigation of the ratio of the EESI-
34 TOF particle signal (M_{diff}) at m/z 185 (C$_6$H$_{10}$O$_5$Na$^+$, corresponding to levoglucosan and its isomers) to
35 that of the AMS C$_2$H$_4$O$_2^+$ (m/z 60) signal, a characteristic fragment of anhydrosugars such as
36 levoglucosan. During a haze period (characterised by large particles with a vacuum aerodynamic
37 diameter (d_{va}) mass distribution centred around 665 nm, Fig. S2), the EESI-TOF:AMS ratio was ~2.
38 In contrast, during a clean period (characterised by smaller particles with a d_{va} mass distribution
39 centred around 302 nm, Fig S2) the EESI-TOF:AMS ratio was ~13 in the AMS. By changing the
40 position of the denuder from 1 cm to 9 cm away from the ESI probe, we increased the ambient signal
41 of m/z 185 (M_{diff}) by a factor of 6 under haze conditions, recovering the EESI-TOF:AMS ratio
42 observed for small particles. Therefore, we positioned the denuder in this campaign about 9 cm away
43 from the probe to avoid size-dependent transmission artefacts. We suggest that the effect of the
44 denuder position on large particle collection is due to the axial velocity profile, which is independent
45 of radial position at the exit of the honeycomb denuder (and nearly so at the 1 cm position) but closer

Atmospheric
Chemistry
and Physics
Discussions

1   to a laminar flow profile at 9 cm. For the 1 cm position, the increased momentum of large particles in
2   the outer regions of the particle flow likely prevents their efficient intersection with the spray and/or
3   subsequent collection into the MS capillary inlet.

4   Data analysis was performed using Tofware version 2.5.7 (Tofwerk AG, Thun, Switzerland). Before
5   high-resolution peak fitting, data were averaged to 2 min. Although EESI-TOF ion signal normally
6   takes only a few seconds to stabilize after a filter switch, in this campaign denuder breakthrough
7   yielded stabilization times from several seconds to several minutes, depending on the ion. Therefore,
8   only the stabilised part of the averaged time series was used for further analysis, corresponding to the
9   last 4 min in the 15 min period of ambient sampling, and the last 2 min in the 5 min filter sampling
10 period, while the remaining time is classified transitional measurements and discarded from further
11 analysis. Adjacent filter sampling periods were linearly interpolated to obtain an estimated M_{filter}
12 corresponding to each M_{total}; the difference of M_{total} minus the interpolated M_{filter} yields the M_{diff}
13 reported here. In total, 2824 ions were identified ranging from m/z 64 to m/z 400. All ions were
14 detected as adducts with Na^+. To facilitate comparison with bulk mass measurements, EESI-TOF
15 signals were converted from counts per second (cps) to the mass flux of ions to the microchannel plate
16 detector (ag s^{-1}), as follows:

17
$$M_x = I_x \times (\mathrm{MW}_x - \mathrm{MW}_{CC}) \tag{2}$$

18 where M_x and I_x are respectively the mass flux of ions in attogrammes per second and the ion flux
19 (cps) reaching the detector for a given ion of identity x . MW_x and MW_{CC} represent the molecular
20 weight of the ion and the charge carrier (e.g. Na^+), respectively (Lopez-Hilfiker et al., 2019; Qi et al.,
21 2019; Stefenelli et al., 2019). This measured mass flux can in principle be converted to ambient
22 concentration by the instrument flow rate, EESI collection efficiency (the probability that the analyte-
23 laden droplet enters the inlet capillary), EESI extraction efficiency (the probability that a molecule
24 dissolves in the spray), ionisation efficiency (the probability that an ion forms and survives
25 declustering forces induced by evaporation and electric fields), and ion transmission efficiency (the
26 probability that a generated ion is transmitted to the detector). However, since several of these
27 parameters are compound-dependent and remain uncharacterised, mass concentration at this stage
28 cannot be determined (Lopez-Hilfiker et al., 2019).

29 The high background signals resulting from denuder breakthrough compromised high-resolution peak
30 fitting of the spectral region containing particle-phase signals in Tofware. Because particle-phase
31 signals tend to be less oxygenated (lower mass defect) than the background ions, a custom peak fitting
32 algorithm (outside of Tofware) was used in which the relative weight of this spectral region was
33 increased, as described in the supplement (see Sect. S1, Fig. S3 and Fig. S4). Further, denuder
34 breakthrough rendered non-trivial the classification of ions as arising primarily from the particle
35 phase, working solution and its impurities vs. gaseous molecules transmitted to the ion source via
36 denuder breakthrough. As only particle-phase ions are desired for further analysis, three criteria were
37 applied for their selection: 1) the ratio of signal to uncertainties, 2) ratio of signal to background and
38 3) estimated saturation vapour mass concentration (C_0) (see Text S2). For criterion (3), only ions
39 having a lower C_0 than levoglucosan were retained. Note that this biases our measurements towards
40 the exclusion of small acids characteristic of aqueous processes.

41 After application of the criteria in Text S2, 401 ions are retained for further analysis. As discussed in
42 Sect. 2.3, source apportionment was conducted on the EESI-TOF data by positive matrix factorization
43 (PMF), which requires as input the mass spectral time series and corresponding uncertainties. The
44 input data matrix $M_{diff}(i, j)$ is calculated according to Eq. (3):

45
$$M_{diff}(i.j) = \mathrm{M}_{total}(i,j) - M_{filter}(i,j) \tag{3}$$

1   where $M_{total}(i,j)$ denotes the signal of spectra measured in total sampling period,

2    $M_{filter,estimate}(i,j)$ denotes signal of estimated background spectra after interpolation of the filter

3   sampling period, and $M_{diff}(i,j)$ denotes signal of the difference spectra between total sampling

4   period and estimated background and consists of 401 (ions) $\times$ 1239 (time points). The error matrix

5   corresponding to M_{diff} is estimated by adding in quadrature the uncertainty of total sampling

6   measurement $\sigma_{total}(i,j)$ and filter sampling measurement $\sigma_{filter,estimate}(i,j)$, which are based on

7   ion counting statistics and detector variability (Allan et al., 2003b), shown in Eq. (4):

8
$$\sigma_{diff}(i,j) = \sqrt{\sigma_{total}^2(i,j) + \sigma_{filter,estimate}^2(i,j)} \tag{4}$$

9

10   2.2.2   Long time-of-flight aerosol mass spectrometer (L-TOF AMS)

11   A long time-of-flight aerosol mass spectrometer (L-TOF AMS, Aerodyne Research Inc.) equipped

12   with a $PM_{2.5}$ aerodynamic lens was deployed to monitor the non-refractory (NR) particle composition

13   with a time resolution of 2 min. The instrument is described in detail elsewhere (Canagaratna et al.,

14   2007). Briefly, particles are sampled continuously at ~0.1 L min^{-1} into a 100 µm critical orifice and

15   then a $PM_{2.5}$ aerodynamic lens, which focuses the particles into a narrow beam and accelerates them to

16   a velocity inversely related to their vacuum aerodynamic diameter (Williams et al., 2013). The

17   particle beam impacts on a heated tungsten surface ~ 600 ℃, and ~ 10^{-7} Torr) and the NR

18   components flash vaporise. The resulting gases are ionised by electron ionisation (EI, ~ 70 eV) and

19   measured by a TOF mass spectrometer. The instrument was calibrated for ionisation efficiency (IE) at

20   the beginning, middle and end of the campaign by a mass-based method using 350 nm NH_4NO_3

21   particles. To eliminate the influence from relative humidity (RH) on collection efficiency (CE), a

22   Polytube Dryer Gas Sample Dryer (Perma Pure LLC) was mounted in front of the AMS inlet. A

23   composition-dependent collection efficiency (CDCE) was applied to correct the measured aerosol

24   mass (Middlebrook et al., 2012). Data analysis was performed in Igor Pro 6.39 (Wavemetrics, Inc.)

25   using SQUIRREL 1.57 and PIKA 1.16 ((Donna Sueper, ToF-AMS high-resolution analysis software).

26   In conventional AMS data analysis, the signal from CO^+ cannot be directly determined due to

27   interference from N_2^+, and is instead assumed to be equal to that of CO_2^+. However, the increased

28   mass resolution provided by the L-TOF detector was sufficient in this study to allow direct peak

29   fitting of CO^+, which is reported herein. As shown by Pieber et al. (2016), CO_2^+ signal in the AMS

30   derives not only from OA and gaseous CO_2, but is also generated directly from the vaporiser in the

31   presence of some inorganic aerosols, notably NH_4NO_3. This effect was corrected using 350 nm

32   NH_4NO_3 aerosol according to the method recommended by Pieber et al. (2016); the nitrate fraction

33   was not high enough to require the composition-dependent method of Freney et al. (2019). The CO_2^+

34   signal resulting from nitrate was found to be 4.4 % of the total CO_2^+ signal. In principle, spurious CO^+

35   signal can be generated by the same process, either through fragmentation of CO_2 or directly via

36   related oxidation reactions. However, the CO^+ signal was below detection limit for the NH_4NO_3 test

37   aerosol. We therefore assumed a value of 0.4 % of total CO^+ signal, which corresponds to 10 % of

38   CO_2^+ as given by the 70 eV EI reference mass spectrum of CO_2 according to the NIST Standard

39   Reference Simulation Website (Shen et al., 2017).

40   Source apportionment (see Sect. 2.3) was performed on the AMS OA data and requires as inputs the

41   OA mass spectral time series and corresponding uncertainties. The data matrix was constructed by

42   including both (1) ions with known molecular formula for $m/z \leq 120$ and (2) the integrated signal

43   across each integer m/z for m/z 121 to m/z 300. This allows inclusion of chemical information at m/z

44   where the number of possible ions and AMS resolution are insufficient for robust identification and

45   quantification of individual ions. Of particular note for the current dataset, inclusion of the high m/z

46   data allows inclusion of polycyclic aromatic hydrocarbons (PAHs) in the PMF analysis. Uncertainties

1   were calculated according to the method of Allan et al. (2003a), and account for electronic noise, ion-

2   to-ion variability at the detector, and ion counting statistics, with a minimum error enforced according

3   to the method of (Ulbrich et al., 2009). As recommended by Paatero and Hopke (2003), variables with

4   weak SNR (0.2<SNR<2) were down-weighted by a factor of 2 and variable with low SNR (SNR<0.2)

5   were removed from input matrices.

6   Ions that were not independently fit but calculated as a constant ratio of CO_2^+ i.e. O^+, HO^+ and H_2O^+,

7   were removed from PMF analysis to avoid overweighting the contribution of CO_2^+. After obtaining

8   the PMF solutions, the contribution of these ions was recalculated and reinserted into the factor

9   profile. The resulting factor profiles were re-normalised, likewise the total mass. Note that although

10   typical AMS source apportionment studies likewise remove CO^+, the increased mass resolution of the

11   LTOF detector allows an independent measurement of CO^+ and this ion is therefore retained for PMF.

12   Isotopes were removed prior to PMF analysis (to avoid overweighting the parent ions) and reinserted

13   afterwards

2.3 Source Apportionment Technique

15   Source apportionment was performed using the positive matrix factorisation (PMF) model,

16   implemented within the multilinear engine (ME-2). AMS and EESI-TOF measurements are highly

17   complementary, with the AMS providing robust quantification but limited chemical resolution, and

18   the EESI-TOF providing a linear but hard-to-quantify response with high chemical resolution. As a

19   result, integrating these two instruments in single source apportionment model represents a promising

20   strategy for improved source apportionment, especially of the SOA fraction. Conceptually, this can be

21   executed in three ways: (1) PMF analysis on a single dataset containing both AMS and EESI-TOF

22   data; (2) PMF analysis of EESI-TOF-only data to identify factors and determine their time series,

23   followed by PMF on AMS-only data with factor time series constrained according to EESI-TOF

24   results; or (3) PMF on AMS-only data to determine factor time series, followed by PMF on EESI-

25   TOF-only data with constrained factor time series to facilitate chemical interpretation of the AMS-

26   determined factors. For the present analysis, we selected method (3) because of EESI-TOF data

27   quality issues related to denuder breakthrough (see Sect. 2.2.1) and the appearance of several

28   interesting-but-unexplained factors in preliminary AMS PMF analysis.

29   For the AMS PMF analysis, one factor related to traffic and one factor related to cooking activities

30   were constrained using the *a* value approach for the HOA spectra from Mohr et al. (2012) and the

31   COA spectra from Crippa et al. (2013). Based on the result from PMF analysis on AMS data, PMF

32   was then performed for the EESI-TOF dataset, by constraining all factor time series retrieved from the

33   first step source apportionment except for the HOA time series (because the hydrocarbon-like species

34   dominating HOA are undetectable by the EESI-TOF extraction/ionization scheme used here). This is

35   conceptually similar to chemical mass balance (CMB), except that here the factor time series are

36   constrained instead of factor profiles. This allows AMS-resolved factors, notably those related to

37   SOA, to be described in terms of the higher chemical resolution achievable by the EESI-TOF. To

38   explore the robustness and uncertainties of each step in our integrated source apportionment,

39   bootstrap analysis was conducted individually on the first step PMF solution from the AMS and the

40   second step "CMB-analogue" result from the EESI-TOF.

41   Determine of the proper number of factors to obtain the most interpretable PMF solution is partly

42   subjective. In this paper, criteria to identify and interpret the factors implemented include to compare

43   the correlation between factor time series or profiles with external references, and to investigate the

44   factor's distinctive chemical signatures. In addition, z-score analysis is introduced to interpret

45   retrieved factor profiles, and demonstrates its advantage in identifying unique ions in each factor.

46   2.3.1   Positive matrix factorisation (PMF)

Atmospheric
Chemistry
and Physics
Discussions

1   Positive matrix factorisation (PMF) was implemented using the Multilinear Engine (ME-2) (Paatero,
2   1997), with model configuration and post-analysis performed with the Source Finder interface (SoFi,
3   version 6.8b) (Canonaco et al., 2013), programmed in Igor Pro 6.39 (Wavemetrics, Inc.). PMF is a
4   bilinear receptor model which describes the input data matrix (here the mass spectral time series) as a
5   linear combination of static factor profiles (in this case characteristic mass spectra, representing
6   specific sources or/and atmospheric processes) and their corresponding time-dependent source
7   contributions, as described in Eq. (5):

8
$$\mathbf{X} = \mathbf{G} \times \mathbf{F} + \mathbf{E} \qquad\qquad (5)$$

9   Here $\mathbf{X}$ is the input data matrix with dimensions of $m \times n$, representing m measurements of n variables
10   (here ions or m/z), $\mathbf{G}$ and $\mathbf{F}$ are respectively the static factor time series with the dimension of $m \times p$,
11   and factor profiles with the dimension of $p \times n$, where p is the number of factors in the PMF solution,
12   and is determined by the user. $\mathbf{E}$ is the residual matrix. $\mathbf{G}$ and $\mathbf{F}$ in Eq. (5) are solved by a least-
13   squares algorithm that iteratively minimises the quantity Q, which is defined in Eq. (6) as the sum of
14   the squares of the uncertainty-weighted residuals:

15
$$Q = \sum_i \sum_j \left(\frac{e_{ij}}{\sigma_{ij}} \right)^2 \qquad\qquad (6)$$

16   Here e_{ij} is an element in the residual matrix $\mathbf{E}$, and σ_{ij} is the corresponding element in the
17   measurement uncertainty matrix, where i and j are the indices representing measurement time and ion
18   (or integer m/z), respectively.

19   PMF is subject to rotational ambiguity, in that different combinations of the $\mathbf{G}$ and $\mathbf{F}$ matrices may
20   yield solutions with the same or similar Q. In practice, this often leads to mixed or unresolvable
21   factors. Here we explore a subset of the possible PMF solutions, directed towards environmentally
22   meaningful rotations. This is achieved via the a-value approach, wherein one or more factor profiles
23   and/or factor time series are constrained using reference factors profiles or/and time series, with the
24   scalar a ($0 \le a \le 1$) determining the tightness of constraint. This approach has been shown to improve
25   solution quality relative to unconstrained PMF (Crippa et al., 2014; Canonaco et al., 2013). The a-
26   value approach determines the extent to which the resolved factor profiles $(g_{i,k})_{solution}$ and time
27   series $(f_{k,j})_{solution}$ may differ from the input values ($g_{i,k}$ or $f_{k,j}$), as shown in Eq. (7a) and Eq. (7b):

28
$$(g_{i,k})_{solution} = g_{i,k} \pm a \times g_{i,k} \qquad\qquad (7a)$$

29
$$(f_{k,j})_{solution} = f_{k,j} \pm a \times f_{k,j} \qquad\qquad (7b)$$

30   Note that the final value of $(g_{i,k})_{solution}$ and $(f_{k,j})_{solution}$ may slightly exceed the prescribed limits
31   due to post-PMF renormalisation of the $\mathbf{G}$ and $\mathbf{F}$ matrices. Here the a-value approach was used for
32   both the AMS and EESI-TOF datasets. Sensitivity tests to determine an appropriate range of a-values
33   were performed in combination with bootstrap analysis, as described in the following section.

34   2.3.2   Bootstrap Analysis
35   Bootstrap analysis (Davison and Hinkley, 1997) was performed to characterise solution stability and
36   estimate uncertainties. Bootstrapping creates a set of new input and error matrices by random
37   resampling of rows from the original input data and error matrices. This resampling preserves the
38   original dimension of input data constant for every single resampling, but randomly duplicates some
39   time points from the original input matrices while excluding others (Paatero et al., 2014). For the
40   AMS dataset, we performed 1000 bootstrap runs on an eight-factor solution, with HOA and COA
41   factors constrained. For each factor, a random a-value was selected for each bootstrap run, ranging
42   from 0 to 0.5 with a step size of 0.1. For the EESI-TOF dataset, 1000 bootstrap runs were performed

1 on a 7-factor solution. Each EESI-TOF factor was constrained by a factor from the AMS 8-factor
2 solution, with AMS HOA excluded because it is not detectable in the EESI-TOF due to low solubility
3 and ionization efficiency. For the EESI-TOF bootstrapping, each factor was constrained with a
4 randomly selected a-value ranging from 0 to 0.6 with a step size of 0.1.

6 Conceptually, each bootstrap solution can be classified in three ways: (1) qualitatively similar to the
7 base case; (2) qualitatively similar to the base case, but with 2 or more factors mixed; (3)
8 fundamentally different from the base case, e.g. one or more factors has appeared and/or disappeared.
9 For characterising uncertainties in the factor profiles and/or time series, only solutions of type (1) are
10 considered. We therefore use the solution classification methods of Stefenelli et al. (2019), which are
11 based on determining whether each factor profile and/or time series from the base case is with
12 statistical significance more similar to one and only one factor in a given bootstrapped solution (with
13 no duplication). This method is implemented in three steps: 1) creation of a base case, 2) Spearman
14 correlation between the time series of each factor from the base case and every bootstrap solution is
15 calculated to sort the bootstrap factors, yielding a correlation matrix with the highest correlation
16 values on the diagonal, 3) each correlation coefficient on the diagonal is compared to values on the
17 row and column to evaluate whether this coefficient is statistically significant higher than other values
18 on the same row or column, by t-test analysis. The bootstrap solutions that fail to meet this criterion
19 are classified as "mixed".

21 The definition of a mixed solution therefore depends on the selected confidence level p, which is
22 evaluated here by a sensitivity test of p ranging from 0.05 to 0.95 with a step of 0.05; the number of
23 solutions classified as "mixed" rises as p increases (Fig. S5). This enables identification of the
24 solutions most likely to be classified as "mixed" for each increment of p. These solutions are
25 manually inspected to confirm that they do in fact appear mixed, and the final p is selected once this
26 no longer holds true. Using this method, a final p of 0.40 for AMS was chosen, yielding 918 accepted
27 bootstrap runs. For EESI-TOF bootstrap analysis, since the time series of all factors are constrained,
28 all runs are considered as good runs and utilised to explore the variability of factor profiles.

30   2.3.3   z-score

31 The dynamic range of EESI-TOF and AMS ion signal concentrations spans several orders of
32 magnitude. It can be that key chemical information is contained in low-intensity ions, which are not
33 readily evident from the factor profile. To assist in identifying such spectral features, we calculate the
34 z-score of each ion across the factor profile matrix as follows:

$$z_{p,g} = (x_{p,g} - \mu_p)/\sigma_p \qquad (8)$$

36 Here $z_{p,g}$ and $x_{p,g}$ is the z-score and the relative intensity of ion p in factor profile g, respectively,
37 and μ_p and σ_p is the mean and standard deviation of relative intensity of ion p in all PMF factors. The
38 Z-score is a signed, dimensionless quantity whose absolute value is to describe the distance between
39 an observation x and population mean μ in the unit of standard deviation σ (Larsen and Marx, 2018).
40 It therefore highlights ions whose contribution to a factor profile is unexpectedly high (or low),
41 independent of absolute signal magnitude. In this study, z-score is used to identify key ions that are
42 unique to a specific factor or small subset of factors, as discussed in Sect. 3.3.

44 **3. Results**
45   **3.1 Campaign overview**

46 During the measurement period, nine haze episodes were observed in total (Fig. 1) from 31 October to
47 5 December. Of these, four haze episodes occurred during the non-heating season, four during the

1   heating season, and one episode bridged the transition date. Consistent with previous studies (Duan et
2   al., 2020; Duan et al., 2019; Zhao et al., 2019; Xu et al., 2019; Sun et al., 2016a; Sun et al., 2016b),
3   alternating haze episodes and clean periods corresponded systematically to changing meteorological
4   conditions. Haze build-up was associated with stagnant air masses with slow wind speed (< 1.5 m s^{-1})
5   mainly from the south or southwest, and terminated by air masses with high wind speed (> 3 m s^{-1})
6   from the north or northwest (Fig. 1b and 1c). Different from previous studies in Beijing in 2014 and
7   2015, where haze events lasting more than five days were observed (Zhao et al., 2019; Xu et al., 2019;
8   Sun et al., 2016b), all haze events in this campaign lasted for two to four days. The maximum
9   concentration of NR-PM$_{2.5}$ measured by the L-TOF AMS exceeded 100 µg m^{-3} in only one haze event
10 (4 to 7 November), and the mean NR-PM$_{2.5}$ concentration in the haze episodes was 36.6 ± 22.7 µg m^{-3}
11 , which is even lower than mean concentrations of NR-PM$_1$ observed in Beijing winter from 2013
12 (89.3 ± 85.6 µg m^{-3}) to 2016 (64 ± 59 µg m^{-3}) (Zhao et al., 2019; Xu et al., 2019; Sun et al., 2016a;
13 Zhang et al., 2014).

14 Aerosol bulk composition differs between the non-heating and heating seasons, indicating changes in
15 sources and/or chemical processes. Organic aerosol (OA) is the major fraction of NR-PM$_{2.5}$
16 throughout the campaign period, with a mean contribution of 54 %, consistent with previous winter
17 studies in Beijing (Zhao et al., 2019; Xu et al., 2019; Elser et al., 2016). The temporal evolution of
18 OA shows that the contribution in haze episodes increased from 41 % during the non-heating season
19 to 54 % during the heating season. This contrasts with nitrate, which is the second largest contributor
20 to NR-PM$_{2.5}$ in this study and contributes 37 % of NR-PM$_{2.5}$ in non-heating season haze events (37 %)
21 but decreases to 23 % during heating season haze events. Of particular note is the non-heating season
22 haze event from 4 to 7 November, where nitrate comprises more than 50 % of NR-PM$_{2.5}$, exceeding
23 OA contribution to total mass in this event. This event is discussed in detail in Sect. 3.3.4 and Sect. 4.
24 It is also worth noticing that the nitrate concentration and its contribution was lower than sulphate
25 during every clean period, but higher during every haze episode. The mean nitrate/sulphate ratio in the
26 present study is 2.8 ± 2.4, a significant increase compared to observations in 2014 (0.7 ± 0.6) and 2016
27 (1.4 ± 0.9) from Xu et al. (2019). In addition, the nitrate/sulphate ratio exceeded 1 for 63 % of
28 measurements in the present study, compared with only 24 % in 2014. It is clear that the contribution
29 of nitrate in haze events gradually exceeded the contribution of sulphate from 2014 to 2017,
30 indicating nitrate is playing an increasingly important role relative to sulphate in haze formation,
31 mainly due to large reduction in SO$_2$ emissions from coal fired power plants in Beijing and
32 surrounding areas.
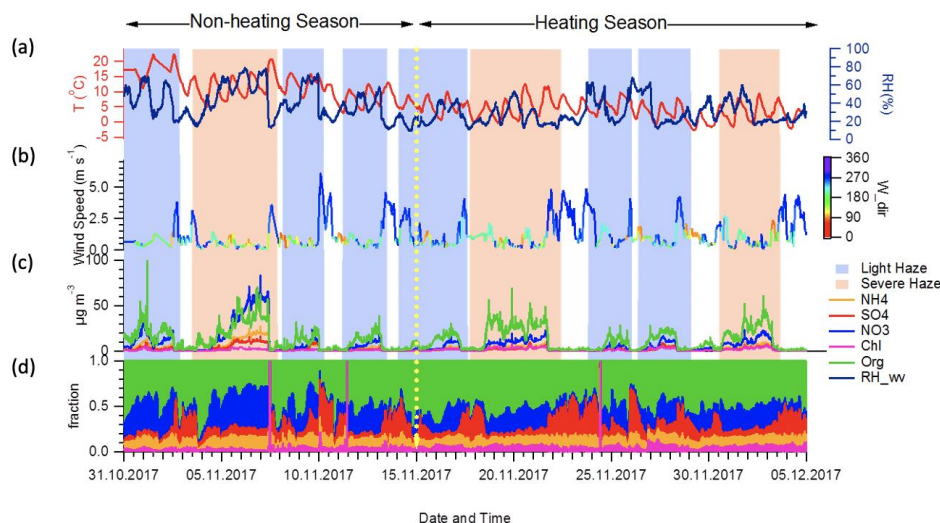
1

2   Figure 1. Time series of meteorological variables and NR-PM$_{2.5}$ composition. (a) temperature (T) and
3   relative humidity (RH), (b) wind speed and wind direction, (c) mass concentrations of NR-PM$_{2.5}$
4   species measured by the AMS, and (d) mass fractions of the species shown in Fig. 1c. Shaded area
5   indicates haze episodes: light haze episodes are defined as having NR-PM$_{2.5}$ concentrations from 20 to
6   150 µg m^{-3} (light blue), while severe haze episodes are defined having NR-PM$_{2.5}$ concentrations above
7   150 µg m^{-3} (light red).

8   **3.2 AMS source apportionment**

9   With the combination of HR ions and UMR sticks in the PMF input matrix, eight factors were
10   resolved, including four primary and four secondary organic factors. Figure 2 shows the averaged MS
11   profiles of the selected eight-factor solution and corresponding relative contribution of each ion (i.e.,
12   fraction of signal from a given ion apportioned to each factor), while Fig. 3 shows the factor time
13   series in terms of both absolute concentration and OA mass fraction. Diurnal patterns are shown in
14   Fig. 3c. The four primary organic factors consist of a traffic related factor (hydrocarbon-like OA,
15   HOA), a cooking related factor (COA), and two solid fuel combustion-related factors (biomass
16   burning OA, BBOA and coal combustion OA, CCOA). The four primary factors retrieved in this
17   solution (HOA, COA, BBOA, and CCOA) have been resolved in several previous winter studies in
18   Beijing (Huang et al., 2014; Elser et al., 2016; Hu et al., 2016; Sun et al., 2016a). However, the SOA
19   factor resolution is unusual. AMS source apportionment studies typically report one or two
20   oxygenated organic aerosol (OOA) factors attributed to SOA, which are distinguished by the extent of
21   oxygenation, which is in turn typically linked to volatility, age, or season. Here, we report four
22   secondary factors, consisting of two more-oxygenated OOAs (MO-OOAs) and two less-oxygenated
23   OOAs (LO-OOAs). For reasons described below and in Sect. 3.3, the MO-OOA factors are attributed
24   to aqueous phase chemistry (MO-OOA$_{aq}$) and solid fuel combustion (MO-OOA$_{SFC}$), while the two
25   LO-OOA factors are attributed to solid fuel combustion (LO-OOA$_{SFC}$), and a non-source-specific
26   factor denoted as (LO-OOA$_{ns}$).

27   In selecting the PMF solution that best represents the AMS dataset, we considered both mathematical
28   diagnostics (e.g. Q/Q_{exp}) as a function of the number and the interpretability of the retrieved factors.
29   Evaluation of factor interpretability includes: 1) correlation of the time series with external data, 2)
30   comparison of factor diurnal cycles with known source activity and previous measurements in
31   Beijing; 3) identification of source-specific spectral features; and 4) differences in factor trends

1 between heating/non-heating and/or haze/non-haze periods. Solutions from five to ten factors were
2 explored (Fig. S7 to Fig. S12), with an eight-factor solution selected as the best representation of the
3 data according to the above criteria. Solutions with less than six factors showed evidence of mixed
4 primary sources. The seven- and eight-factor solutions resolve additional OOA factors, which have
5 clear temporal and compositional differences that support their separation and interpretation.
6 Compared to the eight-factor solution, higher-factor number solutions lead to additional splitting of
7 OOA factors, which cannot be interpreted by previous criteria. Therefore, the eight-factor solution is
8 retained for further analysis.

9 **HOA** -- The HOA spectrum is characterised by alkyl fragments, especially $C_nH_{2n-1}^+$ and $C_nH_{2n+1}^+$.
10 Major ions include $C_3H_7^+$, $C_4H_9^+$, $C_5H_{11}^+$ (Zhao et al., 2019; Xu et al., 2019; Sun et al., 2016a; Elser et
11 al., 2016; Zhang et al., 2014; Ng et al., 2011). It also shows good correlation with CO (Fig. S13),
12 which is a tracer for traffic emissions (Sun et al., 2016a; Zhang et al., 2014; Chan et al., 2011).
13 Concentrations of this factor peak from 06:00 to 09:00 corresponding to the morning rush hour, and
14 from 17:00 to 21:00 in the evening corresponding to evening-night rush hour. The averaged
15 concentration during the evening peak (0.50 µg m^{-3}) is almost twice as high as the morning peak (0.26
16 µg m^{-3}), due to the low planetary boundary layer height and accumulation of vehicle emissions at
17 night (Sun et al., 2016a; Han et al., 2009). This diurnal pattern is consistent with other winter studies
18 in Beijing (Sun et al., 2016a; Zhang et al., 2014). However, the averaged relative contribution of HOA
19 factor to total mass (~3 %) is significantly lower than previous studies (~10 %) (Elser et al., 2016; Hu
20 et al., 2016; Sun et al., 2016a; Zhang et al., 2014; Huang et al., 2010), this indicates that primary
21 traffic emissions comprise a minor fraction of OA during both non-heating and heating periods.

22 **COA** -- The COA spectrum contains both alkyl fragments and slightly oxygenated ions, consistent
23 with aliphatic acids from cooking oils (Hu et al., 2016). It is typically characterised by a ratio of
24 $C_3H_3O^+$ to $C_3H_5O^+$ which greater than 2 and is 3.4 in this study (Xu et al., 2019; Zhao et al., 2019;
25 Sun et al., 2016a; Sun et al., 2016b; Crippa et al., 2013; Mohr et al., 2012). The time series of the
26 COA factor strongly correlates with $C_6H_{10}O^+$ (*m/z* 98), a good tracer for cooking activities reported by
27 many studies (Xu et al., 2019; Zhao et al., 2019; Elser et al., 2016; Hu et al., 2016; Sun et al., 2016a;
28 Sun et al., 2016b; Mohr et al., 2012; Sun et al., 2011), with $r^2 = 0.96$ and 60.1 % of the mass of this
29 ion being apportioned to COA. The diurnal cycle shows three peaks: from 07:00 to 09:00 at breakfast
30 and from 12:00 to 13:00 at lunch time and a larger peak from 18:00 to 21:00 during dinner. This
31 three-peak diurnal pattern agrees with the diurnal cycle observed by Sun et al. (2016a), but differs
32 from many other studies at different sites in winter Beijing where only two peaks are evident and the
33 morning peak from 07:00 to 09:00 is missing, suggesting a dependence on the proximity to local
34 emissions (Xu et al., 2019; Elser et al., 2016; Hu et al., 2016; Zhang et al., 2014). The ratio of dinner
35 peak to lunch peak is about 2, similar to the values of ~2 and 2.3 observed by Elser et al. (2016) and
36 Hu et al. (2016), respectively, whereas Sun et al. (2016a) report a ratio of 1.29. Overall, the COA
37 factor is a non-negligible contributor to total OA, with a relative contribution of 6 %, lower than 18 %
38 in 2013 (Sun et al., 2016a), 25 % in 2014 and 16 % in 2016 wintertime (Xu et al., 2019). The mean
39 concentration is 0.30 µg m^{-3}, lower than previous studies (Xu et al., 2019; Zhao et al., 2019; Elser et
40 al., 2016; Hu et al., 2016; Sun et al., 2016a; Sun et al., 2016b; Mohr et al., 2012; Sun et al., 2011).

41 **BBOA** – Consistent with other studies in Beijing (Zhao et al., 2019; Elser et al., 2016; Hu et al., 2016;
42 Sun et al., 2016a), a BBOA factor was resolved. Typically, the BBOA factor spectrum is
43 characterised by increased contributions from $C_2H_4O_2^+$ at *m/z* 60 and $C_3H_5O_2^+$ at m/z at 73, which is
44 typical of anhydrosugars such as levoglucosan (Alfarra et al., 2007; Lanz et al., 2007; Sun et al.,
45 2011). However, although the contribution of the BBOA factor to $C_2H_4O_2^+$ is the highest (28.6 %)
46 among those factors and its correlation is also high, with $r^2 = 0.62$, other primary sources like CCOA
47 and COA also contribute significant fractions of $C_2H_4O_2^+$ signal. BBOA also correlates strongly with
48 $C_3H_5O_2^+$ ($r^2 = 0.71$) and $C_6H_6O_2^+$ ($r^2 = 0.81$), which are also typical of biomass burning activities
49 (Lanz et al., 2007; Sun et al., 2011). The O:C ratio and N:C ratio of this factor is 0.29 and 0.22,

1 respectively, agreeing quite well with the values found in other studies (Xu et al., 2019; Zhao et al.,
2 2019; Hu et al., 2016).

3 The BBOA time series is event-driven, with both concentrations and relative contributions increasing
4 during haze events, especially the haze event from 18 to 22 November (68.7 % of total OA). Apart
5 from this event, the BBOA concentration increase during other haze events is also clear, regardless of
6 non-heating and heating season. Overall, the average BBOA concentration for the haze events was 1.9
7 $\mu g\ m^{-3}$, with a maximum of 19.1 $\mu g\ m^{-3}$ for the event from 18 to 22 November, and 0.13 $\mu g\ m^{-3}$ for
8 the clean periods, both lower than the study in mid-winter from 2013 to 2014 (Sun et al., 2016a) and
9 the studies covering the same time period of the early winter in 2014 and 2016 (Xu et al., 2019). Its
10 relative contribution to total OA is 15.4 % for haze periods and 8.24 % for the clean period,
11 respectively, consistent to observations of Elser et al. (2016), who report 13.9 % and 8.9 % for haze
12 and clean periods in wintertime in Beijing, respectively.

13 **CCOA** – apart from alkyl fragments $C_nH_{2n-1}^+$ and $C_nH_{2n+1}^+$, the main feature of the CCOA profile is
14 the high contribution from PAHs (approximately m/z 175 to 300), especially in the high m/z range,
15 consistent with studies from Elser et al. (2016), Zhang et al. (2008) and Xu et al. (2006). In the high
16 mass range, PAHs contribute an increasingly higher fraction at higher m/z (Fig. 2b). Strong aromatic
17 and PAH signatures found in the factor profile are at m/z 115 ($C_9H_7^+$), 128, 139, 152, 165, 178, 189,
18 202, 215, 226, 239 and 252 in this study. Moreover, the time series of this factor and these signatures
19 correlate quite well with r^2 of 0.812 ($C_9H_7^+$), 0.801 (m/z 128), 0.834 (m/z 139), 0.903 (m/z 152), 0.906
20 (m/z 165), 0.926 (m/z 178), 0.938 (m/z 189), 0.972 (m/z 202), 0.967 (m/z 215), 0.982 (m/z 226), 0.962
21 (m/z 239) and 0.984 (m/z 252), respectively, consistent with observations from Dzepina et al. (2007),
22 Hu et al. (2013), Hu et al. (2016) and Sun et al. (2016a).

23 Coal is used widely for domestic heating in northern China including the greater Beijing area and
24 surrounding provinces (Zhang et al., 2008), but is not permitted for residential use in the downtown
25 area. Instead, beginning on 15 November, power plants using natural gas provide heating to every
26 household in the Beijing downtown area, and municipal coal combustion begins to provide heating to
27 the surrounding area. Interestingly, the time series of the CCOA factor reflects this seasonal transition,
28 as the mean daily maximum concentration increased from 2.9 $\mu g\ m^{-3}$ before 15 November to 5.9 μg
29 m^{-3} after. Similar to other studies (Elser et al., 2016; Hu et al., 2016; Sun et al., 2016a; Zhang et al.,
30 2014), the diurnal concentration peaks at night between 21:00 and 06:00 with an average contribution
31 of 15.5 % to total OA, and decreases during the day from 07:00 to 20:00 with an average contribution
32 of 7.4 %, consistent with domestic heating. Overall, the mean contribution to total OA is 11.4 %, with
33 7.1 % in the non-heating period and 14.7 % in the heating season. The latter number agrees with
34 observations conducted in the heating period in Beijing during winter, ranging from 10 % to 30 %
35 (Elser et al., 2016; Hu et al., 2016; Zhang et al., 2014; Sun et al., 2013).

36 **OOAs** – As noted above, the OOA factors resolved here differ from previous AMS studies in Beijing,
37 where only one or two OOA factors were resolved and classified based on the volatility (semi-volatile
38 OOA and low-volatility OOA) or oxidation state (more-oxygenated OOA and less-oxygenated OOA).
39 In this study, two more-oxygenated OOAs (MO-OOA) and two less-oxygenated OOA (LO-OOA)
40 were resolved. The OOA factors are characterised by higher signal from CO_2^+ than found in the POA
41 factors. In this study, CO_2^+ comprises approximately 15 % of the two MO-OOA factors. For the two
42 LO-OOAs, the CO_2^+ contribution to the total signal is only 3.78 % in LO-OOA$_{SFC}$ and 5.41 % in LO-
43 OOA$_{ns}$, while the ratio of CO_2^+ to $C_2H_3O^+$ is still higher than it for the POAs. Moreover, a higher
44 contribution of the C_xH_y group is observed in the LO-OOA factors than in the MO-OOA factors. The
45 four OOA factors have significantly different time series, corresponding to specific haze events and/or
46 seasonal changes, providing a first suggestion that their separation may be meaningful.

1   Among the MO-OOA factors, one factor (influenced by aqueous phase chemistry, defined as MO-
2   OOA$_{aq}$) has high absolute and relative concentrations during a single haze event from 4 to 7
3   November (maximum 16.2 µg m^{-3}, > 60 % of the total OA mass), but is a minor component
4   throughout the rest of the campaign. In contrast, the other MO-OOA factor (oxygenated from solid
5   fuel combustion, defined as MO-OOA$_{SFC}$) is a minor component before 15 November, but both its
6   mass and relative contribution steadily increase during the heating season, especially during haze
7   periods. This is consistent with the temporal pattern of CCOA, suggesting this factor may be linked to
8   coal combustion activities. The temporal evolution of the two LO-OOA factors are also
9   distinguishable. The concentration of one factor (LO-OOA$_{SFC}$) increases in every haze episode under
10 stagnant conditions and is correlated with the total OA time series (r^2 =0.91), whereas the other factor
11 (LO-OOA$_{ns}$) exhibits a clear diurnal pattern in the non-heating season, but this diurnal cycle is absent
12 during the heating season. Interestingly, the contribution of the LO-OOA$_{ns}$ factor to total OA is higher
13 during the clean days, suggesting this factor may be more influenced by regional processes. The
14 chemical characteristics and sources/processes governing these OOA factors are discussed in detail in
15 the next section, in conjunction with the EESI-TOF analysis.

16

17

18

(b)

1
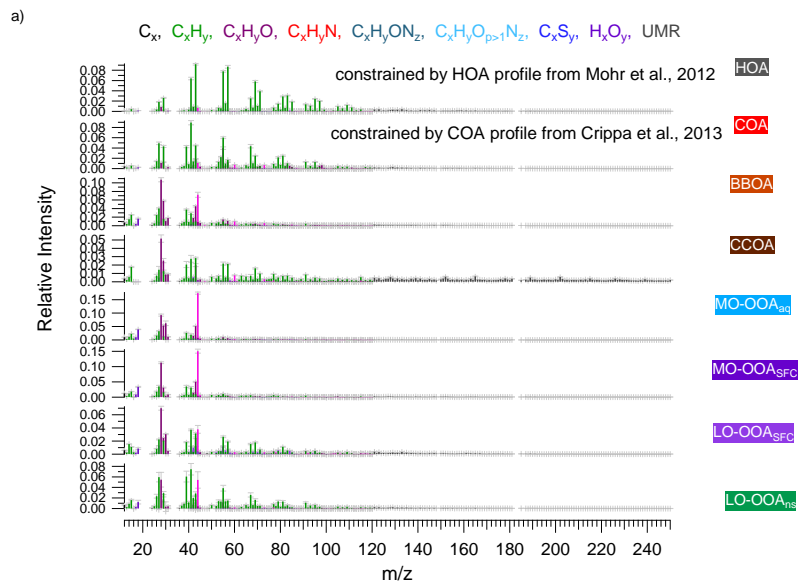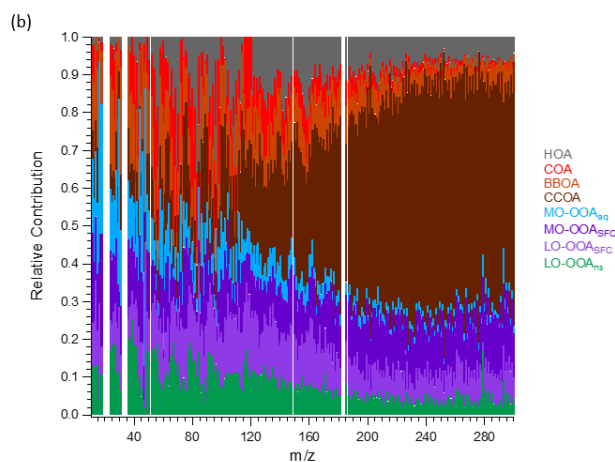
Figure 2. Averaged mass spectra (a) and relative contributions (b) of the 8-factor solution from the AMS PMF bootstrap result. The mass spectra consist of HR ions from m/z 12 to 120, and integrated integer m/z (denoted UMR) from m/z 121 to 300. In (a), error bars denote standard deviation of each stick calculated from all accepted bootstrap solutions.

(a)

6
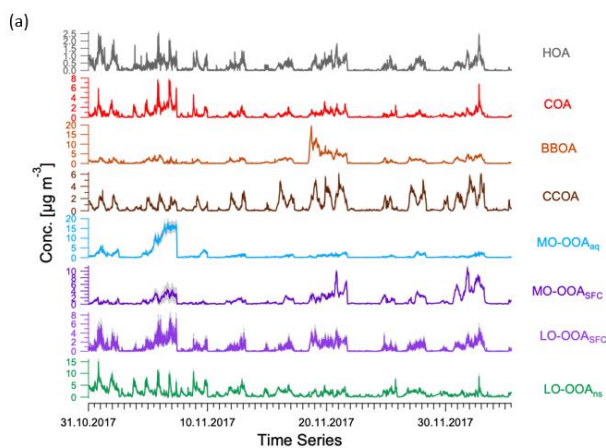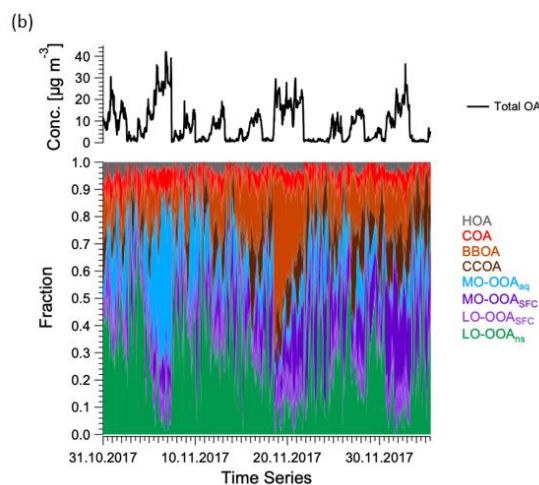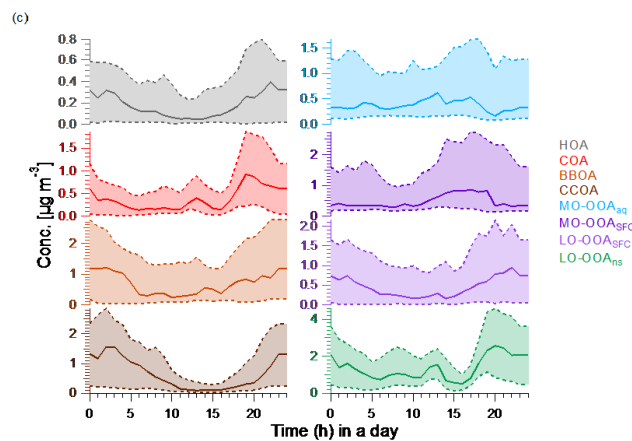
Figure 3. (a) Averaged time series with standard deviations (grey area), (b) averaged total OA concentration and relative contributions and (c) diurnal cycle the accepted AMS PMF bootstrap 8-factor solutions based on the criteria discussed in Sect. 2.3. Lower and upper dashed lines in (c) indicate the 1st and the 3rd quartile.

3.3 Investigation of factor composition by EESI-TOF

As discussed in Sect. 2.3, PMF of the EESI-TOF mass spectral time series was conducted on a 7-factor solution where all factor time series were constrained by the seven non-HOA factors retrieved from AMS PMF. This approach enables a more chemically specific interpretation of the retrieved AMS factors, which both supports POA factor identification and provides additional insight into the sources and processes governing SOA. The PMF result of the EESI-TOF time series was used as the base case for bootstrap runs, and all the bootstrap runs were retained for further analysis. EESI-TOF factor profiles (corresponding to AMS-derived factor time series) are interpreted by 1) comparison between these factor profiles and mass spectra retrieved from a chamber study using an EESI-TOF (Bertrand et al., 2020) and/or field studies (Qi et al., 2019; Stefenelli et al., 2019), 2) identification of key ions in the factor profiles by z-score analysis introduced in Sect. 2.3.3. The time series and factor profiles of the seven-factor solution are shown in Fig. 4.

1   We discuss the three primary factors in Sect. 3.3.1 and the four OOA factors individually in the

2   subsequent sections. For better interpretation, we present carbon number distribution plots from the

3   EESI-TOF factor profiles colour-coded by different families in Fig. 5 and Fig. 6 for the three POA

4   factors, and Figure 5 and Figure 6 for the four OOA factors respectively. In the carbon number

5   distribution plots, ions are classified first based on carbon numbers (x-axis) and ions with same

6   number of carbons are further divided into different categories based on H:C and O:C ratios (colour

7   code). Figure 7 shows Van Krevelen plots (atomic H:C vs. O:C ratio) for the four OOA factors based

8   on AMS factor profiles coloured by number of nitrogen atoms in each fragment, and sized by the

9   median z-score across all bootstrap runs, with large markers denoting ions having z-score > 1.5.

10   ### 3.3.1   POA factors

11 **COA** – Consistent with Qi et al. (2019) and Stefenelli et al. (2019), the mass spectrum of this factor is

12 characterised by having most of the mass at ions with high m/z. These ions at high m/z are likely long-

13 chain fatty acids or/and alcohols related to cooking emission and oils (Liu et al., 2017b). For example,

14 this factor is characterised by long-chain acids like $C_{18}H_{34}O_2^+$, $C_{19}H_{36}O_2^+$ and $C_{21}H_{38}O_3^+$, which

15 apportion 87.2 %, 76.2 %, and 92.3 % of their total mass to this factor, and they are also unique ions

16 in this factor, with z-scores of 2.61, 2.95 and 3.34, respectively.

17 **BBOA** – The mass spectrum of BBOA is characterised by a strong signal at $C_6H_{10}O_5$, corresponding

18 to levoglucosan and its isomers. Levoglucosan is a well-established tracer for primary aerosols

19 formed from pyrolysis of cellulose in biomass burning activities. This ion contributes 6.6 % to the

20 mass in this factor, about 4.5 times higher than the second strongest ion, consistent with previous field

21 and laboratory measurements of biomass burning by the EESI-TOF. Both Qi et al. (2019) (winter

22 measurements in Zurich, Switzerland) and Bertrand et al. (chamber study of wood burning emissions)

23 showed levoglucosan and its isomers to be the dominant ion in EESI-TOF spectra of primary wood

24 burning, with contributions of 13 % and 21 % respectively. In addition, the ion series $C_{10}H_{14}O_x$ ($x \geq 4$)

25 is observed in the BBOA and aged-SFC factors, consistent with Qi et al. (2019).

26 **CCOA** – as shown in the carbon number distribution plots (Figure and Figure), lower H:C and O:C

27 ratios are observed compared to other factors, especially for species with more than 10 carbons, ,

28 suggesting increased contributions from aromatic acids. This is consistent with Zhang et al. (2008)

29 who found that particles generated from industrial boilers typically contain a considerable fraction

30 from both aromatic acids and aliphatic acids. Note that PAHs, which comprise the unique AMS

31 spectral marker, are not detectable by the EESI-TOF extraction/ionisation scheme used here.

(a)

1

(b)
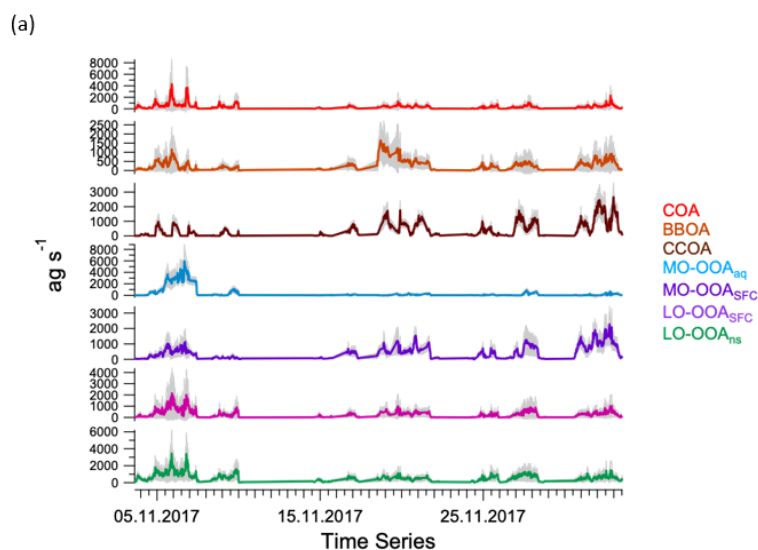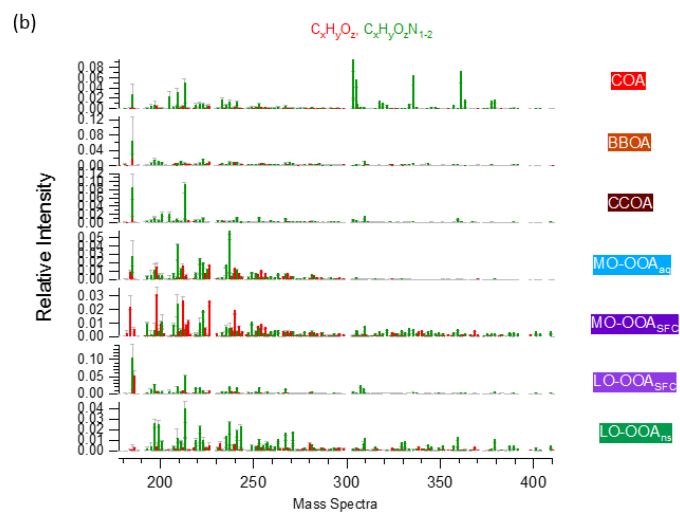
2

3 Figure 4. The averaged (a) time series and (b) mass spectra of accepted solutions from combined
4 bootstrap/*a*-value analysis of the EESI-TOF dataset. EESI-TOF time series are constrained by the 7
5 non-HOA factors retrieved from AMS PMF analysis. Shaded area in (a) indicates the anchor of
6 bootstrap/*a*-value analysis as shown in Eq. (7) and in (b) indicate the standard deviation of each stick
7 calculated from all selected solutions.
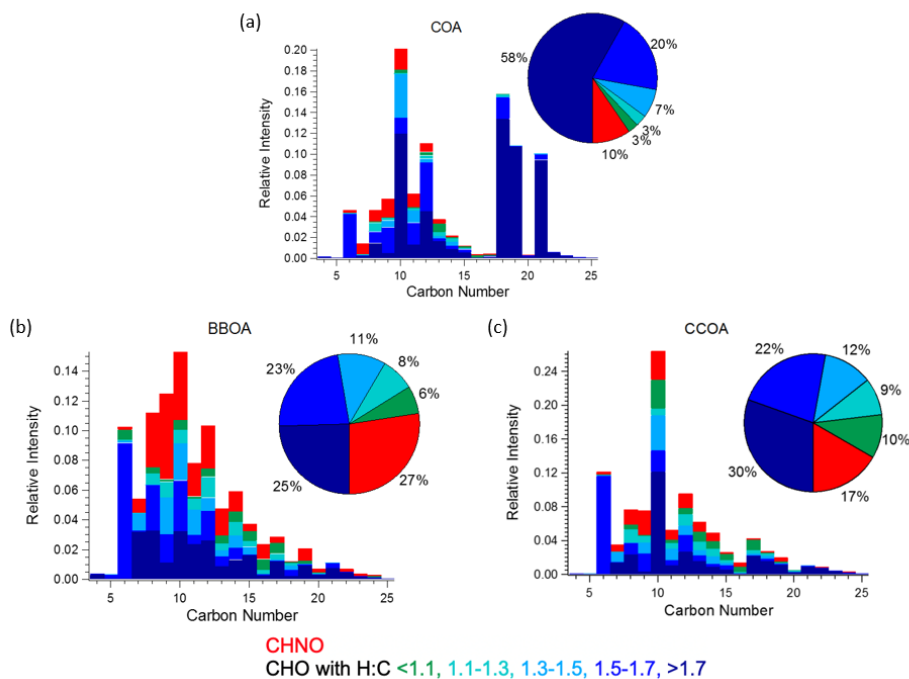
1

2   Figure 5. Carbon number distribution plots of three primary factors coloured by $C_xH_yO_zN_{1-2}$ and five
3   different $C_xH_yO_z$ categories based on H:C ratio (H:C < 1.1, 1.1 < H:C < 1.3, 1.3 < H:C < 1.5, 1.5 <
4   H:C < 1.7 and H:C > 1.7). The sum of each distribution is normalised to 1.

5

20

Atmospheric
Chemistry
and Physics
Discussions
Open Access
EGU
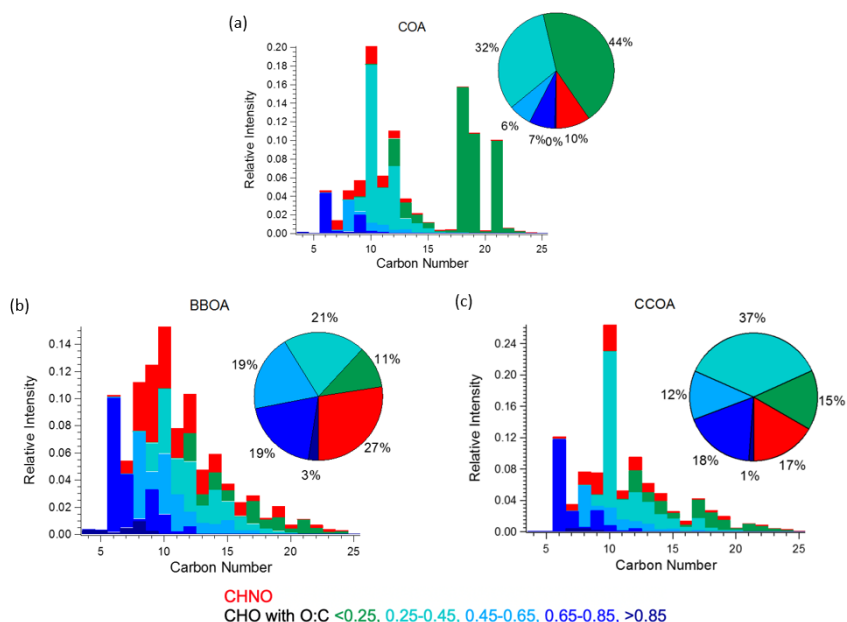
1 Figure 6. Carbon number distribution plots of three primary factors coloured by $C_xH_yO_zN_{1-2}$ and five
2 different $C_xH_yO_z$ categories based on O:C ratio (O:C < 0.25, 0.25 < O:C < 0.45, 0.45 < O:C < 0.65,
3 0.65 < O:C < 0.85 and O:C > 0.85). The sum of each distribution is normalised to 1.

3.3.2 MO-OOA$_{SFC}$

5 As noted in Sect. 3.2, the AMS MO-OOA$_{SFC}$ mass spectrum is consistent with OOA factors
6 characteristic of SOA, and represents aged, oxygenated emissions from solid fuel combustion. The
7 carbon number distribution of the EESI-TOF MO-OOA$_{SFC}$ mass spectrum (Fig. 8b) shows several
8 notable features that provide further insight into its source. First, the contribution of $C_xH_yO_z$ ions with
9 low H:C is significantly higher than for the other OOA factors. Specifically, $(C_xH_yO_z)_{H:C\leq1.3}$ comprises
10 12 % of the total signal and 22 % of $C_xH_yO_z$; for the other non-SFC related OOA factors,
11 $(C_xH_yO_z)_{H:C\leq1.3}$ comprises a maximum of 8 % of the total signal and 10 % of $C_xH_yO_z$. The high
12 fraction from low H:C ratio ions is consistent with other field studies using the EESI-TOF, and
13 suggests a higher contribution from aromatic precursors relative to the other OOA factors. The
14 $(C_xH_yO_z)_{H:C\leq1.3}$ is consistent with that of aged wood burning factors retrieved during winter in Zurich
15 (13-14%, Qi et al., 2019) (Fig. S14). Aged wood burning factors were also retrieved from source
16 apportionment of wintertime EESI-TOF measurements in Magadino, located in a Swiss alpine valley
17 (Stefenelli et al., *in prep*), where $(C_xH_yO_z)_{H:C\leq1.3}$ comprises 9-23 % of the total signal. Different from
18 the aged biomass burning factors found in Zurich and Magadino, $C_6H_{10}O_5$ is not observed in MO-
19 OOA$_{SFC}$, but other ions found in the aged biomass burning factors from Qi et al. (2019) and Stefenelli
20 et al., *in prep* (2019) including $C_{10}H_{16}O_x$ (x = 3,4,5,6…), are also apportioned to SFC-related factors
21 in the present study. Still, the $C_xH_yO_z$ distribution in the MO-OOA$_{SFC}$ factor retrieved in Beijing
22 differs from the previous studies in Switzerland in terms of the overall carbon number distribution.
23 Specifically, the Swiss measurement in Magadino featured by biomass burning activities (Stefenelli,
24 2019) showed a peak at C_6 and a peak from C_8 to C_{10}, the chamber study on coal combustion
25 oxidation (Bertrand et al.) exhibits a peak from C_6 to C_{12} whereas in Beijing the signal is spread over a
26 much larger range (approximately C_7 to C_{19}).

27 Also evident from Fig. 8 is the high contribution from $C_xH_yO_zN_{1-2}$ ions, which comprise ~46 % of the
28 total signal. This is significantly higher than the 18-25 % observed in the Zurich factors by Qi et al.
29 (2019) but comparable to 35-41 % observed in Magadino. As above, the carbon number distribution
30 of $C_xH_yO_zN_{1-2}$ differs between Beijing and Switzerland, although the trends are reversed. In Beijing,
31 the $C_xH_yO_zN_{1-2}$ signal occurs mostly in the C_6 to C_{10} range with a contribution of 73 % to total
32 $C_xH_yO_zN_{1-2}$ signal, whereas for the Swiss measurements it spans C_8 to C_{10} with a contribution of 46 %
33 at most to total $C_xH_yO_zN_{1-2}$ signal and almost evenly distributes into other bins. High intensity
34 $C_xH_yO_zN_{1-2}$ ions in Beijing MO-OOA$_{SFC}$ include $C_6H_{11}NO_4$, $C_7H_{13}NO_4$, $C_8H_{15}NO_4$, $C_9H_{17}NO_4$ and
35 $C_{10}H_{19}NO_4$. The high nitrogen content in MO-OOA$_{SFC}$ likely reflects high NO_x concentrations in the
36 Beijing region during wintertime. In addition, ions tentatively attributed to nitrocatechol ($C_6H_5NO_4$)
37 and its homologous series ($C_7H_7NO_4$, $C_8H_9NO_4$) are apportioned predominantly to this factor and
38 CCOA (see Fig. S16), indicating the influence of oxidised aromatics from coal combustion emissions
39 (Mohr et al., 2013).

40 Interestingly, the AMS MO-OOA$_{SFC}$ profile and Van Krevelen plot (Fig. 7) show that the ions for
41 which MO-OOA$_{SFC}$ has a high z-score (>1.5) predominantly exhibit low H:C ratios. These ions
42 include $C_7H_2O^+$, $C_7H_3O^+$, $C_7H_4O^+$, $C_7H_5O^+$, $C_8H_4O^+$ and $C_8H_5O^+$. Although these ions are not
43 addressed in OOA factor separation in most AMS PMF studies due to their low intensities, their high
44 z-score in the present work suggests they may contain some source-specific information. The
45 temporal evolution of these ions is consistent with the EESI-TOF ions with low H:C ratio, e.g.
46 $C_{12}H_{10}O_8$ and $C_{16}H_{14}O_6$ (see Fig. S16). This also suggests an elevated contribution from aromatic
47 oxidation relative to the non-SFC-derived SOA factors.

3.3.3 LO-OOA$_{SFC}$

1 The LO-OOA$_{SFC}$ factor mass spectrum is also consistent with solid fuel combustion, but is less
2 oxygenated than MO-OOA$_{SFC}$. The carbon number distribution of the EESI-TOF MO-OOA$_{SFC}$ mass
3 spectrum (Fig. 8b) shows a contribution of $C_xH_yO_z$ ions with low H:C comparable to that of MO-
4 OOA$_{SFC}$. Specifically, $(C_xH_yO_z)_{H:C\leq1.3}$ comprises 11 % of the total LO-OOA$_{SFC}$ signal, compared to
5 12 % from MO-OOA$_{SFC}$. This is consistent with less-aged biomass burning (LABB) factors retrieved
6 from source apportionment of wintertime EESI-TOF data in Zurich and Magadino, where
7 $(C_xH_yO_z)_{H:C\leq1.3}$ contributed 10-16 %. LO-OOA$_{SFC}$ contains a substantial contribution (8 %) from
8 $C_6H_{10}O_5$ (levoglucosan and its isomers), which is substantially higher than that of MO-OOA$_{SFC}$ (0 %)
9 and LO-OOA$_{ns}$ (0 %) but lower than for primary BBOA (9 %) and CCOA (12 %). Interestingly, this
10 factor has a very high fraction (32 %) from $(C_xH_yO_z)_{H:C\geq1.7}$, significantly higher than the 12 % to 14 %
11 observed in Zurich and Magadino. It also has 19 % contribution from $(C_xH_yO_z)_{O:C\geq0.65}$, half of the
12 fraction (~40 %) of the LABB factors in Zurich and Magadino. The high H:C (1.66) and low O:C
13 (0.40) from EESI-TOF result in low averaged carbon oxidation states $\overline{OS}_c$ (-0.87) of this factor
14 suggests this factor is less oxygenated than the LABB factors in those two studies, with lowest $\overline{OS}_c$ of
15 -0.60.

16 Regarding nitrogen-containing species, $C_xH_yO_zN_{1-2}$ ions contribute 23 % to the total signal in this
17 factor, similar to their contributions in the Zurich and Magadino LABB (17 % to 22 %). However, in
18 Beijing a large fraction (8 %) of the $C_xH_yO_zN_{1-2}$ derives from a single ion ($C_6H_{11}NO_4$). Otherwise, the
19 carbon number distribution of $C_xH_yO_zN_{1-2}$ ions in Beijing is weighted from C_7 to C_{10}, consistent with
20 SOA from wood burning experiments with OH or NO_3 (Bertrand et al.) as shown in Fig. S17. Similar
21 to the primary BBOA and CCOA factors, LO-OOA$_{SFC}$ is elevated overnight, suggesting a
22 contribution from nighttime chemistry and/or rapid oxidation of primary emissions.

23   3.3.4   MO-OOA$_{aq}$

24 The MO-OOA$_{aq}$ factor time series is dominated by high absolute and relative concentrations during a
25 haze event in the non-heating season. Both the atmospheric conditions during this event and the
26 overall factor composition are consistent with a strong influence from SOA formed by aqueous phase
27 chemistry.

28 Figure 10a shows the time series of the CO_2^+ and CO^+ ions measured by the AMS, with the
29 corresponding scatter plot shown in Fig. 10b. For most of the data, the ratio of CO^+ to CO_2^+ is
30 approximately 1, consistent with the mean CO^+/CO_2^+ value for bulk atmospheric OA (Canagaratna et
31 al., 2015; Aiken et al., 2008) and the assumption in the standard AMS fragmentation table. In
32 contrast, the CO^+/CO_2^+ slope is only 0.5 for the haze event on 4 to 7 November. This relative
33 enhancement of CO_2^+ is characteristic of small acids or diacids, e.g. oxalic acid, malonic acid and
34 succinic acid (Canagaratna et al., 2015). Such molecules are mainly derived from aqueous phase
35 chemistry (Tan et al., 2012; Tan et al., 2010; Carlton et al., 2007; Ervens et al., 2004), although minor
36 contributions might also be possible from soluble species in aerosols formed by gas-phase reactions
37 (Legrand et al., 2005; Sellegri et al., 2003; Sempere and Kawamura, 1994).

38 An enhanced contribution from small acids is also suggested by the EESI-TOF MO-OOA$_{aq}$ profile.
39 As shown in Figs. 7 and 8, MO-OOA$_{aq}$ has enhanced signal from ions with low carbon number
40 relative to the other OOA factors. Further, Fig. 8 shows that these low-C ions are highly oxygenated
41 (e.g. $C_6H_6O_5$), which is likewise consistent with small multifunctional acids and polyacids. The EESI-
42 TOF spectra thus provide further support for the attribution of this factor to SOA generated from
43 aqueous-phase chemistry. Note that due to the application of the volatility-based filter for
44 distinguishing particle-phase vs. spurious ions (see section x), the contribution of such small, highly
45 oxygenated ions presented here represents a lower limit.

46 As shown in Fig. 3, MO-OOA$_{aq}$ provides a major fraction of 41 % to the total OA during the major
47 haze event on 4 to 7 November (peak concentration > 40 µg m^{-3}). In fact, OA concentrations during

1   this event are at least as high as those observed during the heating period, despite the likelihood of
2   reduced concentrations of precursor VOCs due to the mandated reductions in combustion activities
3   related to domestic heating in rural areas. We therefore investigate the reasons for the high aqueous
4   SOA production during this specific event. As aqueous phase chemistry is typically associated with
5   high aerosol liquid water content (LWC), LWC was calculated from ISORROPIA-II (Fountoukis and
6   Nenes, 2007). The LWC concentration is presented in Fig. 10, together with the time series of MO-
7   OOA$_{aq}$. The two time series are strongly correlated (r^2 =of 0.93), and both are dramatically higher
8   during the 4 to 7 November event than for the rest of the study. Note that the strong correlation
9   between MO-OOA$_{aq}$ and LWC is not driven solely by the event on 4 to 7 November; rather, the two
10   time series are remarkably well correlated throughout the entire campaign. This further supports the
11   interpretation of MO-OOA$_{aq}$ as characteristic of aqueous SOA production throughout the campaign,
12   rather than being characteristic of only a single event.

13   The question arises whether MO-OOA$_{aq}$ reflects the irreversible production of SOA via aqueous
14   pathways, or instead reversible solvation of volatile and semivolatile organics. To assess this, we look
15   in detail at the MO-OOA$_{aq}$ and LWC correlations during the 4 to 7 November event. The most
16   significant disagreement between the time series occurs from 08:00 to 23:00 on 6 November, when
17   the LWC sharply decreases while MO-OOA$_{aq}$ remains high. If MO-OOA$_{aq}$ were driven by reversible
18   solvation, this extended decrease in LWC would be expected to drive a corresponding decrease in
19   MO-OOA$_{aq}$. However, the MO-OOA$_{aq}$ concentrations appear unaffected by the decrease in LWC,
20   suggesting that the MO-OOA$_{aq}$ does indeed consist of irreversibly-generated SOA via aqueous
21   chemistry.

22   The reasons for the high LWC are driven by the combination of high RH and high inorganic fraction
23   (especially NH_4NO_3), which as shown in Fig. 1 are both maximised during this period. The high
24   NH_4NO_3 content during 4 to 7 November is in turn driven by a unique airmass source region. Figure
25   11a shows 72-h backward trajectories calculated from the HYSPLIT transport model (Rolph et al.,
26   2017; Stein et al., 2015), and analysed in Zefir v 4.0 (Petit et al., 2017). Trajectories are coloured by
27   date and time. In the figure, trajectories from 4 to 7 November pass over regions of high NO_x
28   emissions to the east and south of Beijing (Shandong and Henan provinces) before arriving at the
29   sampling site. The air parcel spends approximately 30 hours over these high-NO_x regions, as shown in
30   Fig. 11b. As shown in Fig. S18, the period of 4 to 7 November is the only time in the campaign where
31   the back trajectories pass over this region. Due to the high NO_2 concentration and high RH in this
32   period, particulate nitrate is produced during this regional transport homogeneously and/or
33   heterogeneously, resulting in water uptake and high LWC in the aerosol phase. The high LWC in turn
34   facilitates further heterogeneous formation of nitrate. This positive feedback provides favorable
35   conditions for efficient aqueous chemistry and thus production of MO-OOA$_{aq}$ (Kuang et al., 2020).

36   3.3.5   LO-OOA$_{ns}$

37   In Sect. 3.2, this factor has been identified as LO-OOA because of its moderately high CO_2^+ signal
38   and non-negligible contribution from the C_xH_y group. The time series of this factor shows clear
39   diurnal variation which peaks at around 20:00 in the non-heating season (Fig. 3a and 3c), but this
40   variation is not clear in the heating season. In addition, the contribution of this factor to total OA is
41   higher in the clean period than during the haze events (Fig. 3b), indicating this may be related to
42   regional sources/processes rather than more local SFC emissions. The diurnal cycle of this factor is
43   similar to COA and LO-OOA$_{SFC}$, but the chemical characteristics of these three factors are different.
44   Compared to LO-OOA$_{SFC}$, this factor is characterised by ions with high H:C and low O:C and does
45   not have $C_6H_{10}O_5$, a key ion in SFC-related LO-OOAas identified in both the present and previous
46   studies. LO-OOA$_{ns}$ also does not have large contributinos from ions with the aromatic feature of low
47   H:C. Although the spectrum of COA is also characterised by ions with high H:C and low O:C, the
48   carbon number distribution plots of COA are characterised by significant signal from long-chain acids

1   at high carbon number, whereas the carbon number distribution of this factor is characterised by high

2   signal at low carbon number (from C_8 to C_{12}). Compared to other OOA factors, this factor has the

3   lowest O:C ratio (0.33) and highest H:C ratio (1.69). Since it is not characterised by any key ions to

4   our knowledge on previous EESI-TOF studies (e.g. levoglucosan and its isomers), this factor is named

5   as LO-OOA$_{ns}$, representing non-source-specific LO-OOA.
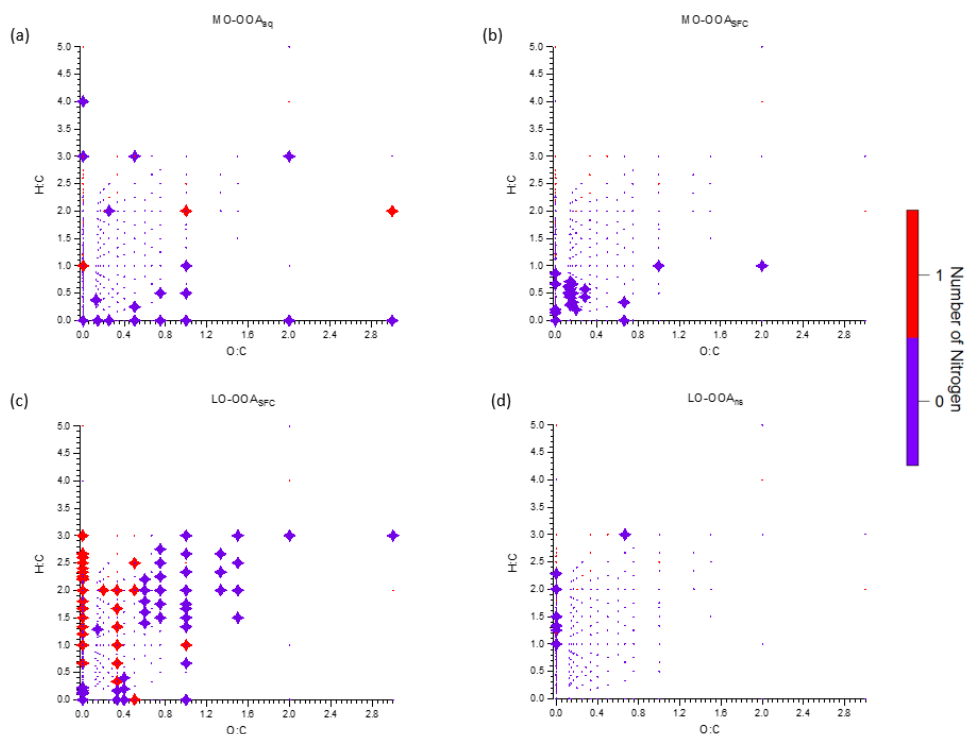
6

7   Figure 4. Van Krevelen plot of (a) MO-OOA$_{aq}$, (b) MO-OOA$_{SFC}$, (c) LO-OOA$_{SFC}$ and (d) LO-OOA$_{ns}$,

8   coloured by the number nitrogen atoms in the AMS fragments. Large symbols denote s with median

9   z-score > 1.5 for accepted runs from bootstrap analysis.
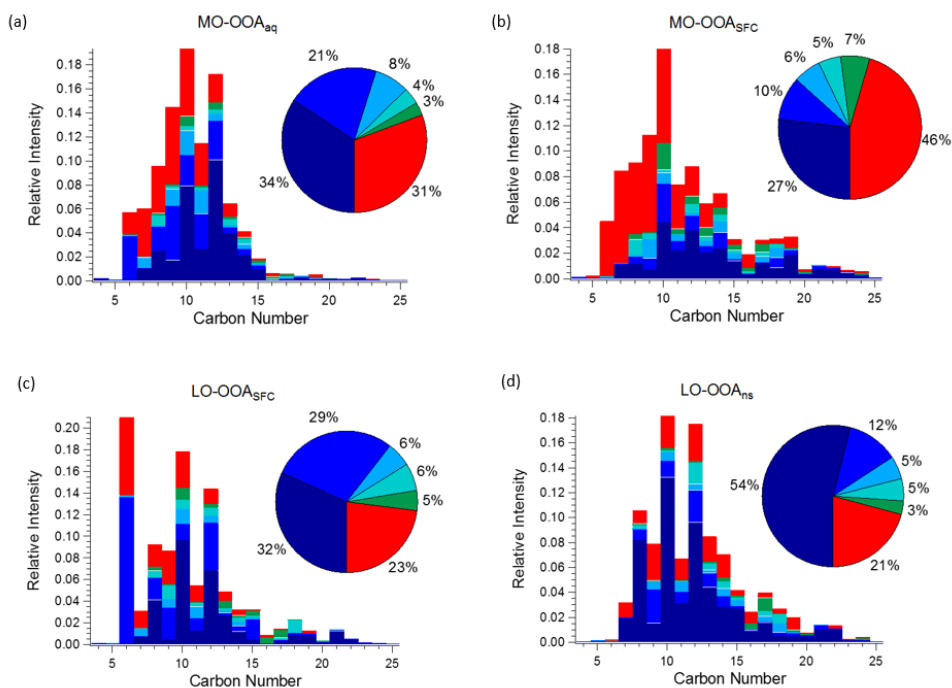
Figure 5. Carbon number distribution plots of four OOA factors coloured by $C_xH_yO_zN_{1-2}$ (red) and five different $C_xH_yO_z$ categories (green to blue) based on H:C ratio (H:C < 1.1, 1.1 < H:C < 1.3, 1.3 < H:C < 1.5, 1.5 < H:C < 1.7 and H:C > 1.7).

1
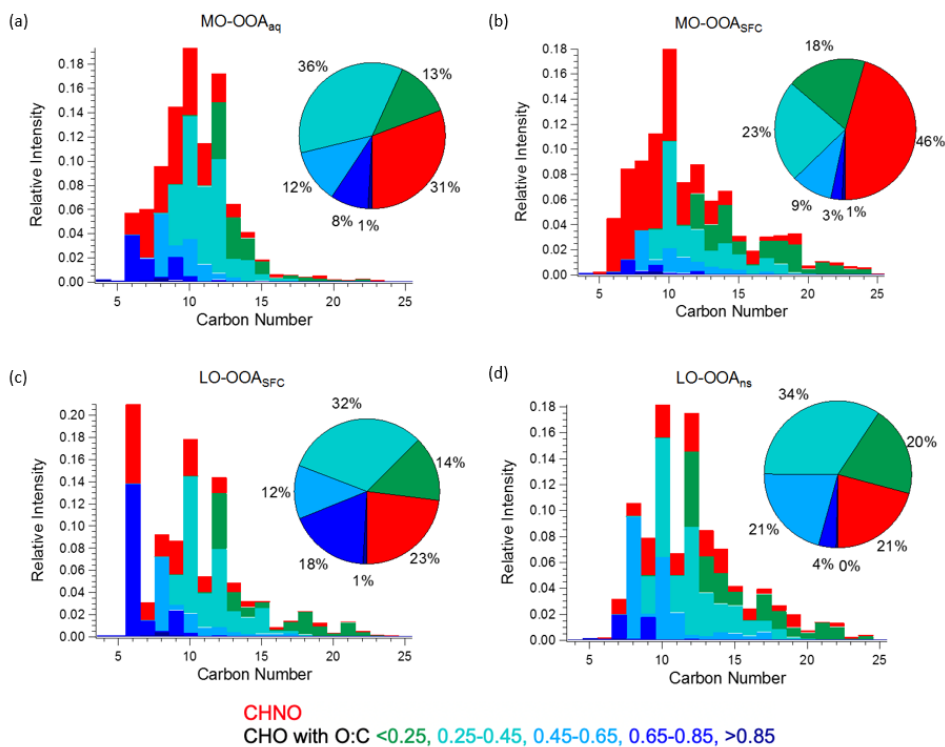
2

Figure 6. Carbon number distribution plots of four OOA factors coloured by $C_xH_yO_zN_{1-2}$ (red) and five different $C_xH_yO_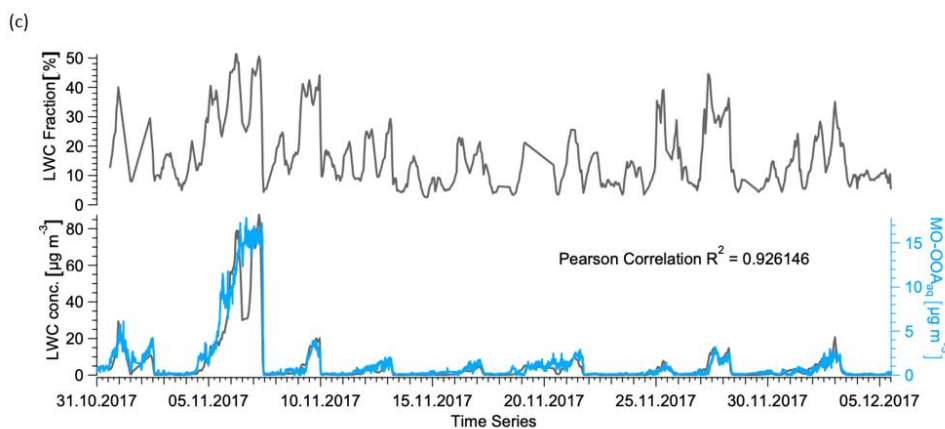z$ categories (green to blue) based on O:C ratio (O:C < 0.25, 0.25 < O:C < 0.45, 0.45 < O:C < 0.65, 0.65 < O:C < 0.85 and O:C > 0.85).

6

7

Atmospheric
Chemistry
and Physics
Discussions
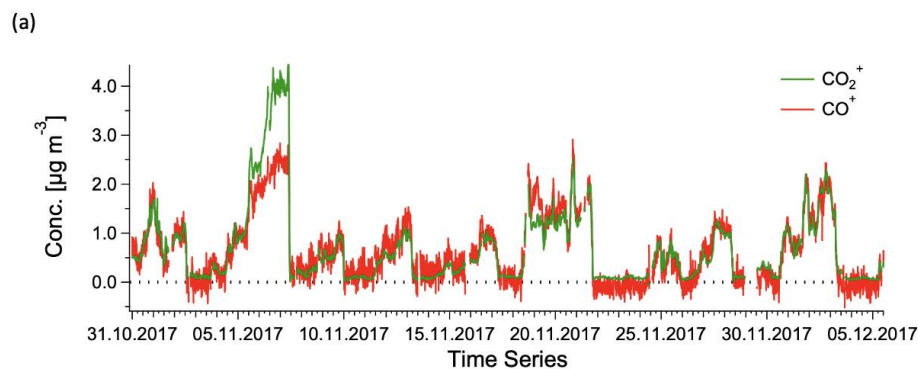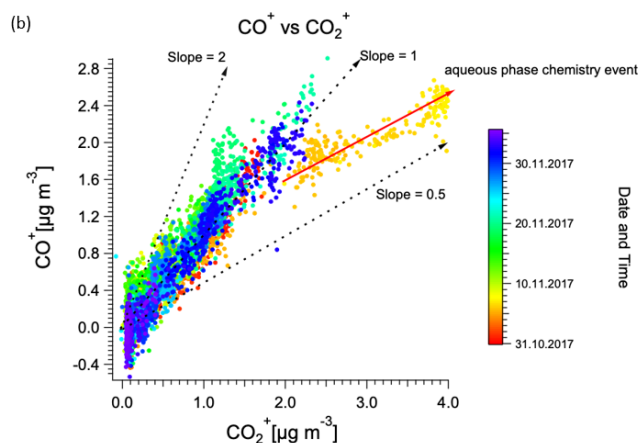
Figure 7. (a) Time series of CO^+ and CO_2^+ throughout the campaign after correction for CO_2^+ contribution from NH_4NO_3 to total CO_2^+ and (b) scatter plot of CO^+ and CO_2^+ indicating a different slope for the haze event between 4 November to 7 November 2017, suggesting aqueous phase chemistry may happen in this period. (c) Time series of LWC, both in fraction (top) and mass concentration (bottom), complemented by $MO\text{-}OOA_{aq}$, demonstrating the high correlation between the latter two variables.
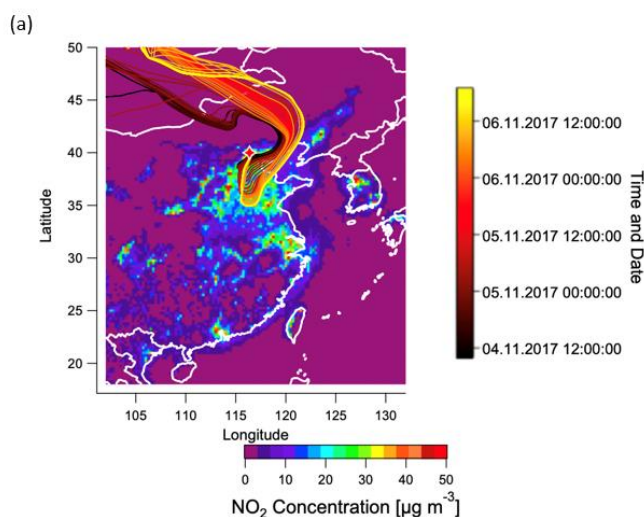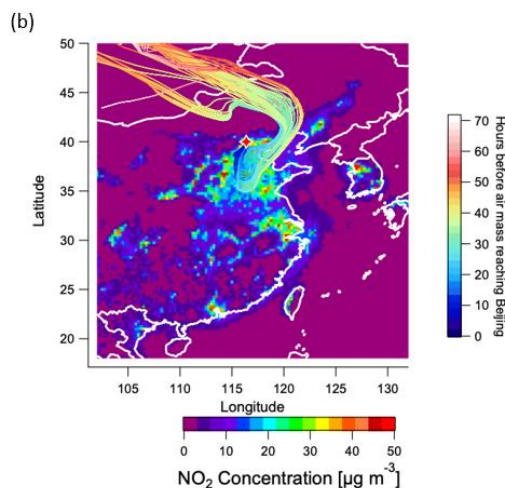
Figure 8. Trajectories analysis. (a) 72-h back-trajectories (HYSPLIT) for the haze event from 4 to 7
November colour-coded by date and time, (b) 72-h back-trajectories for the haze event from 4 to 7
November colour-coded by hours before the air mass reaches Beijing. In both figures, trajectories are
overlaid on a 2015 map of surface NO_2 concentrations based on the CHIMERE model and driven by
the 2015 DECSO inventory (Liu et al., 2018).

4. Atmospheric implications

As discussed in Sect. 3.1, meteorological conditions are responsible for an alternating occurrence of
haze and clean periods and these effects from meteorology are well-understood (Duan et al., 2020;
Duan et al., 2019; Zhao et al., 2019; Xu et al., 2019; Sun et al., 2016a; Sun et al., 2016b). In addition,

Atmospheric
Chemistry
and Physics
Discussions

1   meteorology can also influence air mass trajectories on the regional/mesoscale, which may further
2   influence the aerosol chemical composition. By comparing measurements before and after the start of
3   the heating season (15 November), the effects of heating emissions on clean and haze periods in
4   Beijing can be assessed. Figure 12 shows the time series of total OA and the contribution of different
5   factors to each haze event, suggesting that different seasons are influenced by different
6   sources/processes.

7   Clean periods in both the non-heating and heating seasons are dominated by SOA, comprising 77 %
8   in the non-heating season and 71 % in the heating season. In both seasons, the single largest
9   component is LO-OOA$_{ns}$ (45% and 33% in the non-heating and heating seasons, respectively),
10   consistent with its identification as regional SOA not specific to a single emissions source. The SFC
11   fraction is higher in the heating season, with CCOA and BBOA jointly comprising 22% (vs. 15% in
12   the non-heating season) and LO-OOA$_{SFC}$ and MO-OOA$_{SFC}$ jointly comprising 25% (vs. 19% non-
13   heating).

14   Seasonal differences become more pronounced under haze conditions. Three minor haze events
15   (maximum concentrations between x and y) were observed in each season. During the non-heating
16   season, LO-OOA$_{ns}$ remains the single largest component (33 to 43%), although its fraction is slightly
17   reduced. There is no corresponding fractional increase observed in any of the other factors, but rather
18   an across-the-board relative increase in all, which results in a slightly increased POA fraction (29 to
19   38%, vs. 23% under clean conditions). These changes likely result from an increased role of local
20   emissions and reactivity under the stagnant conditions giving rise to haze. The non-heating minor
21   haze events contrast strongly with the heating minor haze, where there is a larger reduction in the LO-
22   OOA$_{ns}$ fraction (21 to 30%) that corresponds specifically to increased SFC POA (27 to 36%).
23   Interestingly, the SFC SOA fraction is not significantly larger than under clean conditions (21 to
24   26%).

25   In general, the minor haze events within a given season are relatively similar to each other. However,
26   significant differences in composition are observed between the minor and major haze events within a
27   given season. The two major haze events occurring within the heating season are also quite different
28   from each other. The conclusions that can be drawn from this observation are limited by the small
29   number of major haze events sampled (1 non-heating, 2 heating), but suggest the potential for unique
30   meteorological/transport phenomena that may affect sources and composition during the most
31   extreme events. For example, the non-heating haze event (4 to 7 Nov.) is dominated by MO-OOA$_{aq}$
32   from aqueous processes (41% of OA), and as discussed in the previous section corresponds to unique
33   airmass back-trajectories over high-NO$_x$ regions. The event from 18 to 22 Nov. is dominated by SFC,
34   especially BBOA, which comprises 36% of OA (with CCOA contributing an additional 13%), while
35   SFC SOA comprises an only slightly larger fraction (28% of OA) than under clean conditions. In
36   contrast, the major haze event from 30 Nov. to 3 Dec. has a large contribution from both SFC POA
37   (33%) and SFC SOA (40%). Interestingly, the temporal evolution of these two events is also different,
38   with the 18 to 22 Nov. event (high SFC POA) commencing with a sudden concentration increase but
39   remaining relatively stable thereafter, while concentrations during the 30 Nov. to 3 Dec. event (high
40   SFC POA and SOA) increase gradually over multiple days. However, a close inspection of the 18 to
41   22 Nov. event in Fig. 3b shows a decrease in the BBOA fraction and increase in MO-OOA$_{SFC}$ as the
42   event proceeds, suggesting a generally important role for local SOA formation in a stagnant airmass
43   during the course of a haze event.

44   As a conclusion, our observation suggests that the sources and processes giving rise to haze events in
45   Beijing are variable and seasonally-dependent. Two salient features are: 1) in the heating season, SOA
46   formation is driven by oxidation of aromatics from solid fuel combustion (with the contribution from
47   41% to 71% from SFC-related OOA factor to total SOA), 2) under high NO$_x$ and RH conditions,
48   aqueous phase chemistry may have a major contribution to SOA formation (with the contribution of

Atmospheric
Chemistry
and Physics
Discussions

1 54% from MO-OOA$_{aq}$ to total SOA). The combination of high inorganic content and aqueous SOA
2 can yield total mass concentrations comparable to those observed in the heating season, despite
3 reduced regional VOC emissions in the absence of heating processes.

4 Our back-trajectory analysis shows that from 4 to 7 November, the air masses passed through a high
5 NO_2 concentration region and stayed for more than 24 hours in this region (Fig. 11), which facilitated
6 nitrate formation in the aerosol phase and thus water uptake. Therefore, our observation suggests that
7 meteorology cannot only influence the haze evolution on a local scale, but also can have significant
8 effect on aerosol chemistry and chemical composition by influencing the origin and pathway of air
9 mass.

10 From a technical perspective, a surprising outcome of this source apportionment analysis was the
11 extent to which the AMS SOA factor profiles contained source-related information corroborating the
12 chemically more specific measurements of the EESI-TOF. Specifically, the SFC-related factors
13 exhibited systematic enhancements in ions with low H:C ratios, while the CO^+/CO_2^+ ratio clearly
14 higher than 1 was found to be a clear indicator for aqueous-phase chemical processing. Although the
15 latter observation requires the improved mass resolution of the L-ToF-AMS and is therefore not
16 retrievable from most existing AMS datasets, the former suggests that AMS SOA spectra may contain
17 more source-specific information than is typically recognised. Although these results represent a
18 single case study and so should not be overinterpreted, we suggest that intensity-independent
19 statistical tools such as the z-score analysis employed here may be effective in retrieving such
20 information and in providing additional insight into SOA sources. The combination of quantitative
21 AMS data with semi-quantitative EESI-TOF measurements is also shown to be promising, and
22 alternative methods for combining such datasets (e.g. as discussed in the Methods section) should be
23 pursued.

1
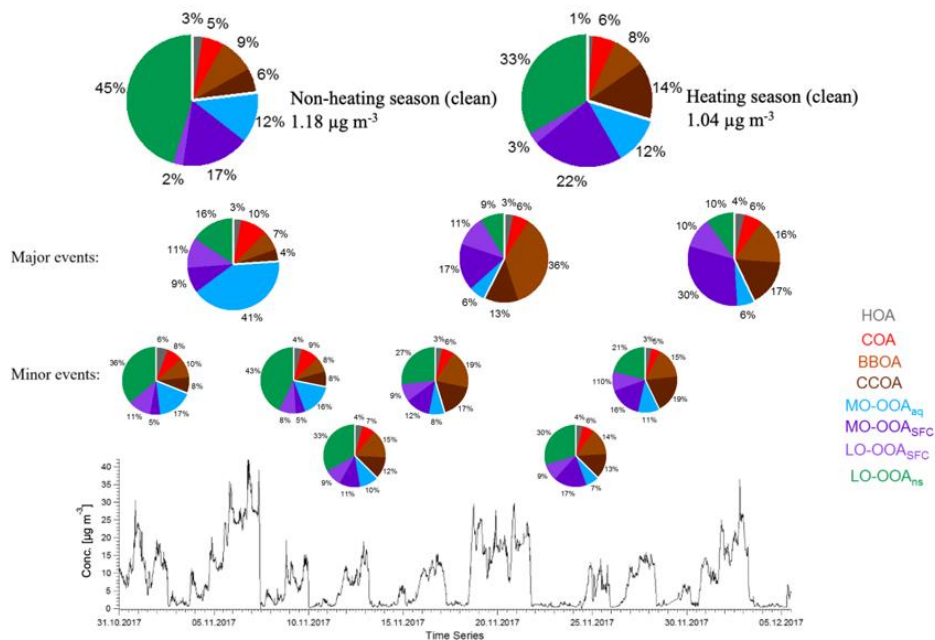
2

3 Figure 9. Time series of total OA and the mean contribution of eight AMS factors in each haze event
4 and clean periods for the non-heating and heating periods. The top two pie charts indicate the
5 averaged contributions for clean periods in non-heating season and heating season.

6

7 **5. Conclusions**

8   OA sources were investigated in Beijing during an intensive field deployment of AMS and EESI-TOF
9   instruments from late September to mid-December 2017, covering the transition from the non-heating
10 to heating seasons. This represents the first deployment of the EESI-TOF in a heavily polluted city.
11 The robust quantification of the AMS and high chemical resolution of the EESI-TOF are shown to be
12 highly complementary, facilitating identification of the sources and processes governing SOA
13 concentrations. An integrated source apportionment study was conducted, by running PMF on AMS-
14 only data first to determine factor time series, followed by PMF on EESI-TOF-only data with
15 constrained factor time series to facilitate chemical interpretation of the AMS-determined factors,
16 which successfully resolved and interpreted four SOA sources and processes.

17 The source apportionment analysis yielded four primary factors and four secondary factors. Primary
18 factors were hydrocarbon-like OA (HOA) characterised by a high fraction of hydrocarbon fragments,
19 cooking-related OA (COA) characterised by long-chain fatty acids, biomass burning OA (BBOA)
20 with a high contribution from levoglucosan, and coal combustion OA (CCOA) with a high PAH
21 signal at high m/z range. The secondary factors consisted of more- and less-oxygenated oxygenated
22 organic aerosol from solid fuel combustion (MO-OOA$_{SFC}$ and LO-OOA$_{SFC}$), more-oxygenated aerosol
23 from aqueous-phase chemistry (MO-OOA$_{aq}$), and less-oxygenated OA from mixed or indeterminate
24 sources (LO-OOA$_{ns}$). The SFC-related factors were characterised by a low H:C ratio in both the
25 EESI-TOF and AMS spectra and increased concentrations during the heating period. MO-OOA$_{aq}$ was
26 characterised by an increased contribution from small, highly oxygenated ions and a low AMS

1 CO^+/CO_2^+ ratio; taken together, these observations suggest an enhanced contribution from small acids
2 and diacids.

3 The OA composition in Beijing is dominated by organic aerosols, with a significant SOA fraction
4 (66.4±13.5 %) to total OA throughout the campaign. SOA formation during the heating season
5 derives mainly from solid fuel combustion. However, even during the non-heating season when solid
6 fuel combustion was not a major source, an intense haze event was observed with OA concentrations
7 comparable to the highest concentrations observed during the heating season. These high
8 concentrations were due to significant SOA production from aqueous phase chemistry, and
9 corresponded to the passage of air parcels over the high NO_x regions to the east and south of Beijing.
10 This suggests that aqueous chemistry may provide a major contribution to SOA formation under
11 certain meteorological conditions, even during periods of intense haze

12

13 *Competing interests*. The authors declare that they have no conflict of interest.

14

27

28 Reference

29 Äijälä, M., Heikkinen, L., Fröhlich, R., Canonaco, F., Prévôt, A. S. H., Junninen, H., Petäjä, T.,
30 Kulmala, M., Worsnop, D., and Ehn, M.: Resolving anthropogenic aerosol pollution types –
31 deconvolution and exploratory classification of pollution events, Atmos. Chem. Phys., 17, 3165-3197,
32 https://doi.org/10.5194/acp-17-3165-2017, 2017.

33 Aiken, A. C., Decarlo, P. F., Kroll, J. H., Worsnop, D. R., Huffman, J. A., Docherty, K. S., Ulbrich, I.
34 M., Mohr, C., Kimmel, J. R., Sueper, D., Sun, Y., Zhang, Q., Trimborn, A., Northway, M., Ziemann,
35 P. J., Canagaratna, M. R., Onasch, T. B., Alfarra, M. R., Prevot, A. S. H., Dommen, J., Duplissy, J.,
36 Metzger, A., Baltensperger, U., and Jimenez, J. L.: O/C and OM/OC ratios of primary, secondary, and
37 ambient organic aerosols with high-resolution time-of-flight aerosol mass spectrometry, Environ Sci
38 Technol, 42, 4478-4485, https://doi.org/10.1021/es703009q, 2008.

39 Alfarra, M. R., Prevot, A. S. H., Szidat, S., Sandradewi, J., Weimer, S., Lanz, V. A., Schreiber, D.,
40 Mohr, M., and Baltensperger, U.: Identification of the mass spectral signature of organic aerosols
41 from wood burning emissions, Environ Sci Technol, 41, 5770-5777,
42 https://doi.org/10.1021/es062289b, 2007.

43 Allan, J. D., Alfarra, M. R., Bower, K. N., Williams, P. I., Gallagher, M. W., Jimenez, J. L.,
44 McDonald, A. G., Nemitz, E., Canagaratna, M. R., Jayne, J. T., Coe, H., and Worsnop, D. R.:
45 Quantitative sampling using an Aerodyne aerosol mass spectrometer: 2. Measurements of fine

1   particulate chemical composition in two UK cities J Geophys Res-Atmos, 108, 4091,
2   https://doi.org/10.1029/2002JD002359, 2003a.

3   Allan, J. D., Jimenez, J. L., Williams, P. I., Alfarra, M. R., Bower, K. N., Jayne, J. T., Coe, H., and
4   Worsnop, D. R.: Quantitative sampling using an Aerodyne aerosol mass spectrometer: 1. Techniques
5   of data interpretation and error analysis (vol 108, art no 4090, 2003), J Geophys Res-Atmos, 108,
6   4090, https://doi.org/10.1029/2002JD002358, 2003b.

7   An, Z., Huang, R.-J., Zhang, R., Tie, X., Li, G., Cao, J., Zhou, W., Shi, Z., Han, Y., Gu, Z., and Ji, Y.:
8   Severe haze in northern China: A synergy of anthropogenic emissions and atmospheric processes,
9   Proceedings of the National Academy of Sciences, 116, 8657-8666,
10   https://doi.org/10.1073/pnas.1900125116, 2019.

11   Beelen, R., Raaschou-Nielsen, O., Stafoggia, M., Andersen, Z. J., Weinmayr, G., Hoffmann, B., Wolf,
12   K., Samoli, E., Fischer, P., Nieuwenhuijsen, M., Vineis, P., Xun, W. W., Katsouyanni, K.,
13   Dimakopoulou, K., Oudin, A., Forsberg, B., Modig, L., Havulinna, A. S., Lanki, T., Turunen, A.,
14   Oftedal, B., Nystad, W., Nafstad, P., De Faire, U., Pedersen, N. L., Ostenson, C. G., Fratiglioni, L.,
15   Penell, J., Korek, M., Pershagen, G., Eriksen, K. T., Overvad, K., Ellermann, T., Eeftens, M., Peeters,
16   P. H., Meliefste, K., Wang, M., Bueno-de-Mesquita, B., Sugiri, D., Kramer, U., Heinrich, J., de
17   Hoogh, K., Key, T., Peters, A., Hampel, R., Concin, H., Nagel, G., Ineichen, A., Schaffner, E., Probst-
18   Hensch, N., Kunzli, N., Schindler, C., Schikowski, T., Adam, M., Phuleria, H., Vilier, A., Clavel-
19   Chapelon, F., Declercq, C., Grioni, S., Krogh, V., Tsai, M. Y., Ricceri, F., Sacerdote, C., Galassi, C.,
20   Migliore, E., Ranzi, A., Cesaroni, G., Badaloni, C., Forastiere, F., Tamayo, I., Amiano, P.,
21   Dorronsoro, M., Katsoulis, M., Trichopoulou, A., Brunekreef, B., and Hoek, G.: Effects of long-term
22   exposure to air pollution on natural-cause mortality: an analysis of 22 European cohorts within the
23   multicentre ESCAPE project, Lancet, 383, 785-795, https://doi.org/10.1016/S0140-6736(13)62158-3,
24   2014.

25   Bertrand, A., Yuan, B., Stefenelli, G., Qi, L., Pospisilova, V., Tong, Y., Sepideh, E., Huang, R. J., El
26   Haddad, I., Slowik, J. G., and Prevot, A.: Characterization of fresh and aged solid fuel combustion
27   organic aerosol by extractive electrospray ionization time-of-flight mass spectrometer (EESI-TOF), in
28   preparation.

29   Bozzetti, C., Sosedova, Y., Xiao, M., Daellenbach, K. R., Ulevicius, V., Dudoitis, V., Mordas, G.,
30   Bycenkiene, S., Bycenkiene, S., Plauskaite, K., Vlachou, A., Golly, B., Chazeau, B., Besombes, J. L.,
31   Baltensperger, U., Jaffrezo, J. L., Slowik, J. G., El Haddad, I., and Prevot, A. S. H.: Argon offline-
32   AMS source apportionment of organic aerosol over yearly cycles for an urban, rural, and marine site
33   in northern Europe, Atmos Chem Phys, 17, 117-141, https://doi.org/10.5194/acp-17-117-2017, 2017.

34   Budisulistiorini, S. H., Canagaratna, M. R., Croteau, P. L., Marth, W. J., Baumann, K., Edgerton, E.
35   S., Shaw, S. L., Knipping, E. M., Worsnop, D. R., Jayne, J. T., Gold, A., and Surratt, J. D.: Real-Time
36   Continuous Characterization of Secondary Organic Aerosol Derived from Isoprene Epoxydiols in
37   Downtown Atlanta, Georgia, Using the Aerodyne Aerosol Chemical Speciation Monitor, Environ Sci
38   Technol, 47, 5686-5694, https://doi.org/10.1021/es400023n, 2013.

39   Canagaratna, M. R., Jayne, J. T., Jimenez, J. L., Allan, J. D., Alfarra, M. R., Zhang, Q., Onasch, T. B.,
40   Drewnick, F., Coe, H., Middlebrook, A., Delia, A., Williams, L. R., Trimborn, A. M., Northway, M.
41   J., DeCarlo, P. F., Kolb, C. E., Davidovits, P., and Worsnop, D. R.: Chemical and microphysical
42   characterization of ambient aerosols with the aerodyne aerosol mass spectrometer, Mass Spectrom
43   Rev, 26, 185-222, https://doi.org/10.1002/mas.20115, 2007.

44   Canagaratna, M. R., Jimenez, J. L., Kroll, J. H., Chen, Q., Kessler, S. H., Massoli, P., Hildebrandt
45   Ruiz, L., Fortner, E., Williams, L. R., Wilson, K. R., Surratt, J. D., Donahue, N. M., Jayne, J. T., and
46   Worsnop, D. R.: Elemental ratio measurements of organic compounds using aerosol mass

1   spectrometry: characterization, improved calibration, and implications, Atmos Chem Phys, 15, 253-
2   272, https://doi.org/10.5194/acp-15-253-2015, 2015.

3   Canonaco, F., Crippa, M., Slowik, J. G., Baltensperger, U., and Prevot, A. S. H.: SoFi, an IGOR-
4   based interface for the efficient use of the generalized multilinear engine (ME-2) for the source
5   apportionment: ME-2 application to aerosol mass spectrometer data, Atmos Meas Tech, 6, 3649-
6   3661, https://doi.org/10.5194/amt-6-3649-2013, 2013.

7   Carlton, A. G., Turpin, B. J., Altieri, K. E., Seitzinger, S., Reff, A., Lim, H. J., and Ervens, B.:
8   Atmospheric oxalic acid and SOA production from glyoxal: Results of aqueous photooxidation
9   experiments, Atmospheric Environment, 41, 7588-7602,
10   https://doi.org/10.1016/j.atmosenv.2007.05.035, 2007.

11   Chan, Y. C., Hawas, O., Hawker, D., Vowles, P., Cohen, D. D., Stelcer, E., Simpson, R., Golding, G.,
12   and Christensen, E.: Using multiple type composition data and wind data in PMF analysis to
13   apportion and locate sources of air pollutants, Atmospheric Environment, 45, 439-449,
14   https://doi.org/10.1016/j.atmosenv.2010.09.060, 2011.

15   Chow, J. C., Bachmann, J. D., Wierman, S. S. G., Mathai, C. V., Malm, W. C., White, W. H.,
16   Mueller, P. K., Kumar, N., and Watson, J. G.: Visibility: Science and regulation - Discussion, J Air
17   Waste Manage, 52, 973-999, https://doi.org/10.1016/j.atmosenv.2010.09.060, 2002.

18   Crippa, M., El Haddad, I., Slowik, J. G., DeCarlo, P. F., Mohr, C., Heringa, M. F., Chirico, R.,
19   Marchand, N., Sciare, J., Baltensperger, U., and Prévôt, A. S. H.: Identification of marine and
20   continental aerosol sources in Paris using high resolution aerosol mass spectrometry, Journal of
21   Geophysical Research: Atmospheres, 118, 1950-1963, https://doi.org/10.1002/jgrd.50151, 2013.

22   Crippa, M., Canonaco, F., Lanz, V. A., Aijala, M., Allan, J. D., Carbone, S., Capes, G., Ceburnis, D.,
23   Dall'Osto, M., Day, D. A., DeCarlo, P. F., Ehn, M., Eriksson, A., Freney, E., Hildebrandt Ruiz, L.,
24   Hillamo, R., Jimenez, J. L., Junninen, H., Kiendler-Scharr, A., Kortelainen, A. M., Kulmala, M.,
25   Laaksonen, A., Mensah, A., Mohr, C., Nemitz, E., O'Dowd, C., Ovadnevaite, J., Pandis, S. N., Petaja,
26   T., Poulain, L., Saarikoski, S., Sellegri, K., Swietlicki, E., Tiitta, P., Worsnop, D. R., Baltensperger,
27   U., and Prevot, A. S. H.: Organic aerosol components derived from 25 AMS data sets across Europe
28   using a consistent ME-2 based source apportionment approach, Atmos Chem Phys, 14, 6159-6176,
29   https://doi.org/10.5194/acp-14-6159-2014, 2014.

30   Daellenbach, K. R., Stefenelli, G., Bozzetti, C., Vlachou, A., Fermo, P., Gonzalez, R., Piazzalunga,
31   A., Colombi, C., Canonaco, F., Hueglin, C., Kasper-Giebl, A., Jaffrezo, J. L., Bianchi, F., Slowik, J.
32   G., Baltensperger, U., El-Haddad, I., and Prevot, A. S. H.: Long-term chemical analysis and organic
33   aerosol source apportionment at nine sites in central Europe: source identification and uncertainty
34   assessment, Atmos Chem Phys, 17, 13265-13282, https://doi.org/10.5194/acp-17-13265-2017, 2017.

35   Davison, A. C., and Hinkley, D. V.: Bootstrap methods and their application, Cambridge University
36   Press, Cambridge, New York, NY, USA, 1997.

37   DeCarlo, P. F., Kimmel, J. R., Trimborn, A., Northway, M. J., Jayne, J. T., Aiken, A. C., Gonin, M.,
38   Fuhrer, K., Horvath, T., Docherty, K. S., Worsnop, D. R., and Jimenez, J. L.: Field-deployable, high-
39   resolution, time-of-flight aerosol mass spectrometer, Anal Chem, 78, 8281-8289,
40   https://doi.org/10.1021/ac061249n, 2006.

41   Duan, J., Huang, R. J., Lin, C., Dai, W., Wang, M., Gu, Y., Wang, Y., Zhong, H., Zheng, Y., Ni, H.,
42   Dusek, U., Chen, Y., Li, Y., Chen, Q., Worsnop, D. R., O'Dowd, C. D., and Cao, J.: Distinctions in
43   source regions and formation mechanisms of secondary aerosol in Beijing from summer to winter,
44   Atmos. Chem. Phys., 19, 10319-10334, https://doi.org/10.5194/acp-19-10319-2019, 2019.

Atmospheric
Chemistry
and Physics
Discussions

1   Duan, J., Huang, R. J., Li, Y., Chen, Q., Zheng, Y., Chen, Y., Lin, C., Ni, H., Wang, M., Ovadnevaite,
2   J., Ceburnis, D., Chen, C., Worsnop, D. R., Hoffmann, T., O'Dowd, C., and Cao, J.: Summertime and
3   wintertime atmospheric processes of secondary aerosol in Beijing, Atmos. Chem. Phys., 20, 3793-
4   3807, https://doi.org/10.5194/acp-20-3793-2020, 2020.

5   Dzepina, K., Arey, J., Marr, L. C., Worsnop, D. R., Salcedo, D., Zhang, Q., Onasch, T. B., Molina, L.
6   T., Molina, M. J., and Jimenez, J. L.: Detection of particle-phase polycyclic aromatic hydrocarbons in
7   Mexico City using an aerosol mass spectrometer, Int J Mass Spectrom, 263, 152-170,
8   https://doi.org/10.1016/j.ijms.2007.01.010, 2007.

9   Eichler, P., Müller, M., D'Anna, B., and Wisthaler, A.: A novel inlet system for online chemical
10   analysis of semi-volatile submicron particulate matter, Atmos. Meas. Tech., 8, 1353-1360,
11   https://doi.org/10.5194/amt-8-1353-2015, 2015.

12   Elser, M., Huang, R. J., Wolf, R., Slowik, J. G., Wang, Q. Y., Canonaco, F., Li, G. H., Bozzetti, C.,
13   Daellenbach, K. R., Huang, Y., Zhang, R. J., Li, Z. Q., Cao, J. J., Baltensperger, U., El-Haddad, I.,
14   and Prevot, A. S. H.: New insights into PM2.5 chemical composition and sources in two major cities
15   in China during extreme haze events using aerosol mass spectrometry, Atmos Chem Phys, 16, 3207-
16   3225, https://doi.org/10.5194/acp-16-3207-2016, 2016.

17   Ervens, B., Feingold, G., Frost, G. J., and Kreidenweis, S. M.: A modeling study of aqueous
18   production of dicarboxylic acids: 1. Chemical pathways and speciated organic mass production, J
19   Geophys Res-Atmos, 109, D15205, https://doi.org/10.1029/2003JD004387, 2004.

20   Fenger, J.: Urban air quality, Atmospheric Environment, 33, 4877-4900,
21   https://doi.org/10.1016/S1352-2310(99)00290-3, 1999.

22   Forster, P., Ramaswamy, V., Artaxo, P., Berntsen, T., Betts, R., Fahey, D.W., Haywood, J., Lean, J.,
23   Lowe, D.C., Myhre, G., Nganga, J., Prinn, R., Raga, G., Schulz, M. and Van Dorland, R.: Changes in
24   Atmospheric Constituents and in Radiative Forcing. In: Climate Change 2007: The Physical Science
25   Basis. Contribution of Working Group I to the Fourth Assessment Report of the Intergovernmental
26   Panel on Climate Change [Solomon, S., Qin, D., Manning, M., Chen, Z., Marquis, M., Averyt, K.B.,
27   Tignor, M. and Miller, H.L. (eds.)]. Cambridge University Press, Cambridge, United Kingdom and
28   New York, NY, USA, 2007.

29   Fountoukis, C. and Nenes, A.: ISORROPIA II: a computationally efficient thermodynamic
30   equilibrium model for $K^+–Ca^{2+}–Mg^{2+}–NH_4^+–Na^+–SO_4^{2-}–NO_3^-–Cl^-–H_2O$ aerosols, Atmos. Chem.
31   Phys., 7, 4639–4659, https://doi.org/10.5194/acp-7-4639-2007, 2007.

32   Freney, E., Zhang, Y. J., Croteau, P., Amodeo, T., Williams, L., Truong, F., Petit, J. E., Sciare, J.,
33   Sarda-Esteve, R., Bonnaire, N., Arumae, T., Aurela, M., Bougiatioti, A., Mihalopoulos, N., Coz, E.,
34   Artinano, B., Crenn, V., Elste, T., Heikkinen, L., Poulain, L., Wiedensohler, A., Herrmann, H.,
35   Priestman, M., Alastuey, A., Stavroulas, I., Tobler, A., Vasilescu, J., Zanca, N., Canagaratna, M.,
36   Carbone, C., Flentje, H., Green, D., Maasikmets, M., Marmureanu, L., Minguillon, M. C., Prevot, A.
37   S. H., Gros, V., Jayne, J., and Favez, O.: The second ACTRIS inter-comparison (2016) for Aerosol
38   Chemical Speciation Monitors (ACSM): Calibration protocols and instrument performance
39   evaluations, Aerosol Sci Tech, 53, 830-842, https://doi.org/10.1080/02786826.2019.1608901, 2019.

40   Ge, X. L., Setyan, A., Sun, Y. L., and Zhang, Q.: Primary and secondary organic aerosols in Fresno,
41   California during wintertime: Results from high resolution aerosol mass spectrometry, J Geophys
42   Res-Atmos, 117, D19201, https://doi.org/10.1029/2012JD018026, 2012.

43   Halliwell, B., and Cross, C. E.: Oxygen-Derived Species - Their Relation to Human-Disease and
44   Environmental-Stress, Environ Health Persp, 102, 5-12, https://doi.org/10.1289/ehp.94102s105, 1994.

Hallquist, M., Wenger, J. C., Baltensperger, U., Rudich, Y., Simpson, D., Claeys, M., Dommen, J.,
Donahue, N. M., George, C., Goldstein, A. H., Hamilton, J. F., Herrmann, H., Hoffmann, T., Iinuma,
Y., Jang, M., Jenkin, M. E., Jimenez, J. L., Kiendler-Scharr, A., Maenhaut, W., McFiggans, G.,
Mentel, T. F., Monod, A., Prevot, A. S. H., Seinfeld, J. H., Surratt, J. D., Szmigielski, R., and Wildt,
J.: The formation, properties and impact of secondary organic aerosol: current and emerging issues,
Atmos Chem Phys, 9, 5155-5236, https://doi.org/10.5194/acp-9-5155-2009, 2009.

Han, S., Kondo, Y., Oshima, N., Takegawa, N., Miyazaki, Y., Hu, M., Lin, P., Deng, Z., Zhao, Y.,
Sugimoto, N., and Wu, Y.: Temporal variations of elemental carbon in Beijing, J Geophys Res-
Atmos, 114, D23202, https://doi.org/10.1029/2009JD012027, 2009.

Hildebrandt, L., Engelhart, G. J., Mohr, C., Kostenidou, E., Lanz, V. A., Bougiatioti, A., DeCarlo, P.
F., Prevot, A. S. H., Baltensperger, U., Mihalopoulos, N., Donahue, N. M., and Pandis, S. N.: Aged
organic aerosol in the Eastern Mediterranean: the Finokalia Aerosol Measurement Experiment-2008,
Atmos Chem Phys, 10, 4167-4186, https://doi.org/10.5194/acp-10-4167-2010, 2010.

Hu, W. W., Hu, M., Yuan, B., Jimenez, J. L., Tang, Q., Peng, J. F., Hu, W., Shao, M., Wang, M.,
Zeng, L. M., Wu, Y. S., Gong, Z. H., Huang, X. F., and He, L. Y.: Insights on organic aerosol aging
and the influence of coal combustion at a regional receptor site of central eastern China, Atmos.
Chem. Phys., 13, 10095-10112, https://doi.org/10.5194/acp-13-10095-2013, 2013.

Hu, W. W., Hu, M., Hu, W., Jimenez, J. L., Yuan, B., Chen, W. T., Wang, M., Wu, Y. S., Chen, C.,
Wang, Z. B., Peng, J. F., Zeng, L. M., and Shao, M.: Chemical composition, sources, and aging
process of submicron aerosols in Beijing: Contrast between summer and winter, J Geophys Res-
Atmos, 121, 1955-1977, https://doi.org/10.1002/2015JD024020, 2016.

Huang, R. J., Zhang, Y. L., Bozzetti, C., Ho, K. F., Cao, J. J., Han, Y. M., Daellenbach, K. R., Slowik,
J. G., Platt, S. M., Canonaco, F., Zotter, P., Wolf, R., Pieber, S. M., Bruns, E. A., Crippa, M., Ciarelli,
G., Piazzalunga, A., Schwikowski, M., Abbaszade, G., Schnelle-Kreis, J., Zimmermann, R., An, Z. S.,
Szidat, S., Baltensperger, U., El Haddad, I., and Prevot, A. S. H.: High secondary aerosol contribution
to particulate pollution during haze events in China, Nature, 514, 218-222,
https://doi.org/10.1038/nature13774, 2014.

Huang, X. F., He, L. Y., Hu, M., Canagaratna, M. R., Sun, Y., Zhang, Q., Zhu, T., Xue, L., Zeng, L.
W., Liu, X. G., Zhang, Y. H., Jayne, J. T., Ng, N. L., and Worsnop, D. R.: Highly time-resolved
chemical characterization of atmospheric submicron particles during 2008 Beijing Olympic Games
using an Aerodyne High-Resolution Aerosol Mass Spectrometer, Atmos Chem Phys, 10, 8933-8945,
https://doi.org/10.5194/acp-10-8933-2010, 2010.

Jimenez, J. L., Canagaratna, M. R., Donahue, N. M., Prevot, A. S. H., Zhang, Q., Kroll, J. H.,
DeCarlo, P. F., Allan, J. D., Coe, H., Ng, N. L., Aiken, A. C., Docherty, K. S., Ulbrich, I. M.,
Grieshop, A. P., Robinson, A. L., Duplissy, J., Smith, J. D., Wilson, K. R., Lanz, V. A., Hueglin, C.,
Sun, Y. L., Tian, J., Laaksonen, A., Raatikainen, T., Rautiainen, J., Vaattovaara, P., Ehn, M.,
Kulmala, M., Tomlinson, J. M., Collins, D. R., Cubison, M. J., Dunlea, E. J., Huffman, J. A., Onasch,
T. B., Alfarra, M. R., Williams, P. I., Bower, K., Kondo, Y., Schneider, J., Drewnick, F., Borrmann,
S., Weimer, S., Demerjian, K., Salcedo, D., Cottrell, L., Griffin, R., Takami, A., Miyoshi, T.,
Hatakeyama, S., Shimono, A., Sun, J. Y., Zhang, Y. M., Dzepina, K., Kimmel, J. R., Sueper, D.,
Jayne, J. T., Herndon, S. C., Trimborn, A. M., Williams, L. R., Wood, E. C., Middlebrook, A. M.,
Kolb, C. E., Baltensperger, U., and Worsnop, D. R.: Evolution of Organic Aerosols in the
Atmosphere, Science, 326, 1525-1529, https://doi.org/10.1126/science.1180353, 2009.

Junninen, H., Ehn, M., Petäjä, T., Luosujärvi, L., Kotiaho, T., Kostiainen, R., Rohner, U., Gonin, M.,
Fuhrer, K., Kulmala, M., and Worsnop, D. R.: A high-resolution mass spectrometer to measure
atmospheric ion composition, Atmos. Meas. Tech., 3, 1039-1053, https://doi.org/10.5194/amt-3-1039-
2010, 2010.

1 Krapf, M., Kunzi, L., Allenbach, S., Bruns, E. A., Gavarini, I., El-Haddad, I., Slowik, J. G., Prevot, A.
2 S. H., Drinovec, L., Mocnik, G., Dumbgen, L., Salathe, M., Baumlin, N., Sioutas, C., Baltensperger,
3 U., Dommen, J., and Geiser, M.: Wood combustion particles induce adverse effects to normal and
4 diseased airway epithelia, Environ Sci-Proc Imp, 19, 538-548, https://doi.org/10.1039/c6em00586a,
5 2017.

6 Kuang, Y., He, Y., Xu, W., Yuan, B., Zhang, G., Ma, Z., Wu, C., Wang, C., Wang, S., Zhang, S., Tao,
7 J., Ma, N., Su, H., Cheng, Y., Shao, M., and Sun, Y.: Photochemical Aqueous-Phase Reactions Induce
8 Rapid Daytime Formation of Oxygenated Organic Aerosol on the North China Plain, Environ Sci
9 Technol, https://doi.org/10.1021/acs.est.9b06836, 2020.

10 Laden, F., Schwartz, J., Speizer, F. E., and Dockery, D. W.: Reduction in fine particulate air pollution
11 and mortality - Extended follow-up of the Harvard six cities study, Am J Resp Crit Care, 173, 667-
12 672, https://doi.org/10.1164/rccm.200503-443OC, 2006.

13 Lanz, V. A., Alfarra, M. R., Baltensperger, U., Buchmann, B., Hueglin, C., and Prévôt, A. S. H.:
14 Source apportionment of submicron organic aerosols at an urban site by factor analytical modelling of
15 aerosol mass spectra, Atmos. Chem. Phys., 7, 1503-1522, https://doi.org/10.5194/acp-7-1503-2007,
16 2007.

17 Larsen, R. J., and Marx, M. L.: An introduction to mathematical statistics and its applications, Sixth
18 edition. ed., Pearson, Boston, MA, USA, 2018.

19 Legrand, M., Preunkert, S., Galy-Lacaux, C., Liousse, C., and Wagenbach, D.: Atmospheric year-
20 round records of dicarboxylic acids and sulfate at three French sites located between 630 and 4360 m
21 elevation, J Geophys Res-Atmos, 110, D13302, https://doi.org/10.1029/2004JD005515, 2005.

22 Li, N., Sioutas, C., Cho, A., Schmitz, D., Misra, C., Sempf, J., Wang, M. Y., Oberley, T., Froines, J.,
23 and Nel, A.: Ultrafine particulate pollutants induce oxidative stress and mitochondrial damage,
24 Environ Health Persp, 111, 455-460, https://doi.org/10.1289/ehp.6000, 2003.

25 Liu, F., Ronald, J. V., Eskes, H., Ding, J. Y., and Mijling, B.: Evaluation of modeling NO_2
26 concentrations driven by satellite-derived and bottom-up emission inventories using in situ
27 measurements over China, Atmos Chem Phys, 18, 4171-4186, https://doi.org/10.5194/acp-18-4171-
28 2018, 2018.

29 Liu, J. C., Wilson, A., Mickley, L. J., Dominici, F., Ebisu, K., Wang, Y., Sulprizio, M. P., Peng, R.
30 D., Yue, X., Son, J. Y., Anderson, G. B., and Bell, M. L.: Wildfire-specific Fine Particulate Matter
31 and Risk of Hospital Admissions in Urban and Rural Counties, Epidemiology, 28, 77-85,
32 https://doi.org/10.1097/EDE.0000000000000556, 2017a.

33 Liu, T., Li, Z., Chan, M., and Chan, C. K.: Formation of secondary organic aerosols from gas-phase
34 emissions of heated cooking oils, Atmos. Chem. Phys., 17, 7333-7344, https://doi.org/10.5194/acp-
35 17-7333-2017, 2017b.

36 Lohmann, U., and Feichter, J.: Global indirect aerosol effects: a review, Atmos Chem Phys, 5, 715-
37 737, https://doi.org/10.5194/acp-5-715-2005, 2005.

38 Lopez-Hilfiker, F. D., Mohr, C., Ehn, M., Rubach, F., Kleist, E., Wildt, J., Mentel, T. F., Lutz, A.,
39 Hallquist, M., Worsnop, D., and Thornton, J. A.: A novel method for online analysis of gas and
40 particle composition: description and evaluation of a Filter Inlet for Gases and AEROsols
41 (FIGAERO), Atmos. Meas. Tech., 7, 983-1001, https://doi.org/10.5194/amt-7-983-2014, 2014.

42 Lopez-Hilfiker, F. D., Pospisilova, V., Huang, W., Kalberer, M., Mohr, C., Stefenelli, G., Thornton, J.
43 A., Baltensperger, U., Prevot, A. S. H., and Slowik, J. G.: An extractive electrospray ionization time-

1   of-flight mass spectrometer (EESI-TOF) for online measurement of atmospheric aerosol particles,
2   Atmos Meas Tech, 12, 4867-4886, https://doi.org/10.5194/amt-12-4867-2019, 2019.

3   Mayer, H.: Air pollution in cities, Atmospheric Environment, 33, 4029-4037,
4   https://doi.org/10.1016/S1352-2310(99)00144-2, 1999.

5   Middlebrook, A. M., Bahreini, R., Jimenez, J. L., and Canagaratna, M. R.: Evaluation of
6   Composition-Dependent Collection Efficiencies for the Aerodyne Aerosol Mass Spectrometer using
7   Field Data, Aerosol Sci Tech, 46, 258-271, https://doi.org/10.1080/02786826.2011.620041, 2012.

8   Mohr, C., DeCarlo, P. F., Heringa, M. F., Chirico, R., Slowik, J. G., Richter, R., Reche, C., Alastuey,
9   A., Querol, X., Seco, R., Penuelas, J., Jimenez, J. L., Crippa, M., Zimmermann, R., Baltensperger, U.,
10 and Prevot, A. S. H.: Identification and quantification of organic aerosol from cooking and other
11 sources in Barcelona using aerosol mass spectrometer data, Atmos Chem Phys, 12, 1649-1665,
12 https://doi.org/10.5194/acp-12-1649-2012, 2012.

13 Mohr, C., Lopez-Hilfiker, F. D., Zotter, P., Prévôt, A. S., Xu, L., Ng, N. L., Herndon, S. C., Williams,
14 L. R., Franklin, J. P., and Zahniser, M. S.: Contribution of nitrated phenols to wood burning brown
15 carbon light absorption in Detling, United Kingdom during winter time, Environ Sci Technol, 47,
16 6316-6324, https://doi.org/10.1021/es400683v, 2013.

17 Muller, M., Eicher, P., D'Anna, B., Tan, W., and Wisthaler, A.: Direct Sampling and Analysis of
18 Atmospheric Particulate Organic Matter by Proton-Transfer-Reaction Mass Spectrometry, Anal
19 Chem, 89, 10889-10897, https://doi.org/10.1021/acs.analchem.7b02582, 2017.

20 Myhre, G., Shindell, D., Bréon, F.-M., Collins, W., Fuglestvedt, J., Huang, J., Koch, D., Lamarque, J.-
21 F., Lee, D., Mendoza, B., Nakajima, T., Robock, A., Stephens, G., Takemura, T., and Zhang, H.:
22 Anthropogenic and Natural Radiative Forcing. In: Climate Change 2013: The Physical Science Basis.
23 Contribution of Working Group I to the Fifth Assessment Report of the Intergovernmental Panel on
24 Climate Change [Stocker, T.F., Qin, D., Plattner, G.-K., Tignor, M., Allen, S.K., Boschung, J.,
25 Nauels, A., Xia, Y., Bex, V. and Midgley, P.M. (eds.)]. Cambridge University Press, Cambridge,
26 United Kingdom and New York, NY, USA, 2013.

27 Ng, N. L., Canagaratna, M. R., Jimenez, J. L., Zhang, Q., Ulbrich, I. M., and Worsnop, D. R.: Real-
28 Time Methods for Estimating Organic Component Mass Concentrations from Aerosol Mass
29 Spectrometer Data, Environ Sci Technol, 45, 910-916, https://doi.org/10.1021/es102951k, 2011.

30 Paatero, P.: Least squares formulation of robust non-negative factor analysis, Chemometr Intell Lab,
31 37, 23-35, https://doi.org/10.1016/S0169-7439(96)00044-5, 1997.

32 Paatero, P., and Hopke, P. K.: Discarding or downweighting high-noise variables in factor analytic
33 models, Anal Chim Acta, 490, 277-289, https://doi.org/10.1016/S0003-2670(02)01643-4, 2003.

34 Paatero, P., Eberly, S., Brown, S. G., and Norris, G. A.: Methods for estimating uncertainty in factor
35 analytic solutions, Atmos Meas Tech, 7, 781-797, https://doi.org/10.5194/amt-7-781-2014, 2014.

36 Penner, J. E., Xu, L., and Wang, M. H.: Satellite methods underestimate indirect climate forcing by
37 aerosols, P Natl Acad Sci USA, 108, 13404-13408, https://doi.org/10.1073/pnas.1018526108, 2011.

38 Petit, J. E., Favez, O., Albinet, A., and Canonaco, F.: A user-friendly tool for comprehensive
39 evaluation of the geographical origins of atmospheric pollution: Wind and trajectory analyses,
40 Environ Modell Softw, 88, 183-187, https://doi.org/10.1016/j.envsoft.2016.11.022, 2017.

41 Pieber, S. M., El Haddad, I., Slowik, J. G., Canagaratna, M. R., Jayne, J. T., Platt, S. M., Bozzetti, C.,
42 Daellenbach, K. R., Frohlich, R., Vlachou, A., Klein, F., Dommen, J., Miljevic, B., Jimenez, J. L.,

Atmospheric
Chemistry
and Physics
Discussions

1   Worsnop, D. R., Baltensperger, U., and Prevot, A. S. H.: Inorganic Salt Interference on CO_2^+ in
2   Aerodyne AMS and ACSM Organic Aerosol Composition Studies, Environ Sci Technol, 50, 10494-
3   10503, https://doi.org/10.1021/acs.est.6b01035, 2016.

4   Pope, C. A., Burnett, R. T., Thun, M. J., Calle, E. E., Krewski, D., Ito, K., and Thurston, G. D.: Lung
5   cancer, cardiopulmonary mortality, and long-term exposure to fine particulate air pollution, Jama-J
6   Am Med Assoc, 287, 1132-1141, https://doi.org/10.1001/jama.287.9.1132, 2002.

7   Qi, L., Chen, M. D., Stefenelli, G., Pospisilova, V., Tong, Y. D., Bertrand, A., Hueglin, C., Ge, X. L.,
8   Baltensperger, U., Prevot, A. S. H., and Slowik, J. G.: Organic aerosol source apportionment in
9   Zurich using an extractive electrospray ionization time-of-flight mass spectrometer (EESI-TOF-MS) -
10 Part 2: Biomass burning influences in winter, Atmos Chem Phys, 19, 8037-8062,
11 https://doi.org/10.5194/acp-19-8037-2019, 2019.

12 Reuter, S., Gupta, S. C., Chaturvedi, M. M., and Aggarwal, B. B.: Oxidative stress, inflammation, and
13 cancer How are they linked?, Free Radical Bio Med, 49, 1603-1616,
14 https://doi.org/10.1016/j.freeradbiomed.2010.09.006, 2010.

15 Rolph, G., Stein, A., and Stunder, B.: Real-time Environmental Applications and Display sYstem:
16 READY, Environ Modell Softw, 95, 210-228, https://doi.org/10.1016/j.envsoft.2017.06.025, 2017.

17 Sellegri, K., Laj, P., Marinoni, A., Dupuy, R., Legrand, M., and Preunkert, S.: Contribution of
18 gaseous and particulate species to droplet solute composition at the Puy de Dome, France, Atmos
19 Chem Phys, 3, 1509-1522, https://doi.org/10.5194/acp-3-1509-2003, 2003.

20 Sempere, R., and Kawamura, K.: Comparative Distributions of Dicarboxylic-Acids and Related Polar
21 Compounds in Snow Rain and Aerosols from Urban Atmosphere, Atmospheric Environment, 28,
22 449-459, https://doi.org/10.1016/1352-2310(94)90123-6, 1994.

23 Shen, V. K., Siderius, D. W., Krekelberg, W. P., and Hatch, H. W.: NIST standard reference
24 simulation website, NIST Standard Reference Database, 2014-2017,
25 https://doi.org/10.18434/T4M88Q, 2017.

26 Stefenelli, G., Bertrand, A., Yuan, B., Qi, L., Pospisilova, V., Lopez-Hilfiker, F. D., Hueglin, C.,
27 Baltensperger, U., Prévôt, A. S. H., and Slowik, J. G.: Laboratory and field investigation of biomass
28 burning aerosol aging using an extractive electrospray ionization time-of-flight mass spectrometer
29 (EESI-TOF), in preparation.

30 Stefenelli, G., Pospisilova, V., Lopez-Hilfiker, F. D., Daellenbach, K. R., Hüglin, C., Tong, Y.,
31 Baltensperger, U., Prévôt, A. S. H., and Slowik, J. G.: Organic aerosol source apportionment in
32 Zurich using an extractive electrospray ionization time-of-flight mass spectrometer (EESI-TOF-MS) –
33 Part 1: Biogenic influences and day–night chemistry in summer, Atmos. Chem. Phys., 19, 14825-
34 14848, https://doi.org/10.5194/acp-19-14825-2019, 2019.

35 Stein, A. F., Draxler, R. R., Rolph, G. D., Stunder, B. J. B., Cohen, M. D., and Ngan, F.: Noaa's
36 Hysplit Atmospheric Transport and Dispersion Modeling System, B Am Meteorol Soc, 96, 2059-
37 2077, https://doi.org/10.1175/BAMS-D-14-00110.1, 2015.

38 Sun, Y. L., Zhang, Q., Schwab, J. J., Demerjian, K. L., Chen, W. N., Bae, M. S., Hung, H. M.,
39 Hogrefe, O., Frank, B., Rattigan, O. V., and Lin, Y. C.: Characterization of the sources and processes
40 of organic and inorganic aerosols in New York city with a high-resolution time-of-flight aerosol mass
41 apectrometer, Atmos. Chem. Phys., 11, 1581-1602, https://doi.org/10.5194/acp-11-1581-2011, 2011.

1   Sun, Y. L., Wang, Z. F., Fu, P. Q., Yang, T., Jiang, Q., Dong, H. B., Li, J., and Jia, J. J.: Aerosol
2   composition, sources and processes during wintertime in Beijing, China, Atmos. Chem. Phys., 13,
3   4577-4592, https://doi.org/10.5194/acp-13-4577-2013, 2013.

4   Sun, Y. L., Du, W., Fu, P. Q., Wang, Q. Q., Li, J., Ge, X. L., Zhang, Q., Zhu, C. M., Ren, L. J., Xu,
5   W. Q., Zhao, J., Han, T. T., Worsnop, D. R., and Wang, Z. F.: Primary and secondary aerosols in
6   Beijing in winter: sources, variations and processes, Atmos Chem Phys, 16, 8309-8329,
7   https://doi.org/10.5194/acp-16-8309-2016, 2016a.

8   Sun, Y. L., Wang, Z. F., Wild, O., Xu, W. Q., Chen, C., Fu, P. Q., Du, W., Zhou, L. B., Zhang, Q.,
9   Han, T. T., Wang, Q. Q., Pan, X. L., Zheng, H. T., Li, J., Guo, X. F., Liu, J. G., and Worsnop, D. R.:
10 "APEC Blue": Secondary Aerosol Reductions from Emission Controls in Beijing, Sci Rep-Uk, 6,
11 20668, https://doi.org/10.1038/srep20668 (2016), 2016b.

12 Tan, Y., Carlton, A. G., Seitzinger, S. P., and Turpin, B. J.: SOA from methylglyoxal in clouds and
13 wet aerosols: Measurement and prediction of key products, Atmospheric Environment, 44, 5218-
14 5226, https://doi.org/10.1016/j.atmosenv.2010.08.045, 2010.

15 Tan, Y., Lim, Y., Altieri, K., Seitzinger, S., and Turpin, B.: Mechanisms leading to oligomers and
16 SOA through aqueous photooxidation: insights from OH radical oxidation of acetic acid and
17 methylglyoxal, Atmos Chem Phys, 12, 801, https://doi.org/10.5194/acp-12-801-2012, 2012.

18 Ulbrich, I. M., Canagaratna, M. R., Zhang, Q., Worsnop, D. R., and Jimenez, J. L.: Interpretation of
19 organic components from Positive Matrix Factorization of aerosol mass spectrometric data, Atmos
20 Chem Phys, 9, 2891-2918, https://doi.org/10.5194/acp-9-2891-2009, 2009.

21 Williams, B. J., Goldstein, A. H., Kreisberg, N. M., and Hering, S. V.: An In-Situ Instrument for
22 Speciated Organic Composition of Atmospheric Aerosols: Thermal Desorption Aerosol GC/MS-FID
23 (TAG), Aerosol Sci Tech, 40, 627-638, https://doi.org/10.1080/02786820600754631, 2006.

24 Williams, L. R., Gonzalez, L. A., Peck, J., Trimborn, D., McInnis, J., Farrar, M. R., Moore, K. D.,
25 Jayne, J. T., Robinson, W. A., Lewis, D. K., Onasch, T. B., Canagaratna, M. R., Trimborn, A., Timko,
26 M. T., Magoon, G., Deng, R., Tang, D., Blanco, E. D. L. R., Prevot, A. S. H., Smith, K. A., and
27 Worsnop, D. R.: Characterization of an aerodynamic lens for transmitting particles greater than 1
28 micrometer in diameter into the Aerodyne aerosol mass spectrometer, Atmos Meas Tech, 6, 3271-
29 3280, https://doi.org/10.5194/amt-6-3271-2013, 2013.

30 Xu, S. S., Liu, W. X., and Tao, S.: Emission of polycyclic aromatic hydrocarbons in China, Environ
31 Sci Technol, 40, 702-708, https://doi.org/10.1021/es0517062, 2006.

32 Xu, W. Q., Sun, Y. L., Wang, Q. Q., Zhao, J., Wang, J. F., Ge, X. L., Xie, C. H., Zhou, W., Du, W.,
33 Li, J., Fu, P. Q., Wang, Z. F., Worsnop, D. R., and Coe, H.: Changes in Aerosol Chemistry From 2014
34 to 2016 in Winter in Beijing: Insights From High-Resolution Aerosol Mass Spectrometry, J Geophys
35 Res-Atmos, 124, 1132-1147, https://doi.org/10.1029/2018JD029245, 2019.

36 Zhang, J. K., Sun, Y., Liu, Z. R., Ji, D. S., Hu, B., Liu, Q., and Wang, Y. S.: Characterization of
37 submicron aerosols during a month of serious pollution in Beijing, 2013, Atmos Chem Phys, 14,
38 2887-2903, https://doi.org/10.5194/acp-14-2887-2014, 2014.

39 Zhang, Y. X., Schauer, J. J., Zhang, Y. H., Zeng, L. M., Wei, Y. J., Liu, Y., and Shao, M.:
40 Characteristics of particulate carbon emissions from real-world Chinese coal combustion, Environ Sci
41 Technol, 42, 5068-5073, https://doi.org/10.1021/es7022576, 2008.

42 Zhao, J., Qiu, Y. M., Zhou, W., Xu, W. Q., Wang, J. F., Zhang, Y. J., Li, L. J., Xie, C. H., Wang, Q.
43 Q., Du, W., Worsnop, D. R., Canagaratna, M. R., Zhou, L. B., Ge, X. L., Fu, P. Q., Li, J., Wang, Z.

1   F., Donahue, N. M., and Sun, Y. L.: Organic Aerosol Processing During Winter Severe Haze
2   Episodes in Beijing, J Geophys Res-Atmos, 124, 10248-10263,
3   https://doi.org/10.1029/2019JD030832, 2019.

4